

1 **A muographic study of a scoria cone from 11**
2 **directions using nuclear emulsion cloud chambers**

3

4 Seigo Miyamoto¹, Shogo Nagahara^{1,2}, Kunihiro Morishima³, Toshiyuki Nakano³,
5 Masato Koyama⁴, Yusuke Suzuki⁵

6

7 ¹Earthquake Research Institute, The University of Tokyo, 1-1-1 Yayoi, Bunkyo-ku,
8 Tokyo, 113-0032, Japan.

9 ²Graduate School of Human Development and Environment, Kobe University, 3-11
10 Tsurukabuto, Nada-ku, Kobe, Hyogo, 657-8501, Japan.

11 ³Fundamental Particle Physics Laboratory, Graduate School of Science of Nagoya
12 University, Furocho, Chikusa-ku, Nagoya, Aichi, 464-8602, Japan.

13 ⁴DeCenter for Integrated Research and Education of Natural Hazardspartment of
14 Education, Shizuoka University, 836 Ohya, Suruga-ku, Shizuoka City, Shizuoka,
15 Japan.

16 ⁵STORY, Ltd., 2-2-5-2321, Minatomachi, Naniwa-ku, Osaka City, Osaka, Japan.

17 *Correspondence to:* Seigo Miyamoto (miyamoto@eri.u-tokyo.ac.jp)

コメントの追加 [宮本 成悟1]: Modification of co-
author's institute

18 **Abstract**

19 One of the key challenges for muographic studies is to reveal the detailed 3D density
20 structure of a volcano by increasing the number of observation directions. 3D density
21 imaging by multi-directional muography requires that the individual differences in the
22 performance of the installed muon detectors are small and that the results from each
23 detector can be derived without any bias in the data analysis. Here we describe a pilot
24 muographic study of the Izu–Omuroyama scoria cone in Shizuoka Prefecture, Japan,
25 from 11 directions, using a new nuclear emulsion detector design optimized for quick
26 installation in the field. We describe the details of the data analysis and present a
27 validation of the results.

28 The Izu–Omuroyama scoria cone is an ideal target for the first multi-directional
29 muographic study, given its expected internal density structure and the topography
30 around the cone. We optimized the design of the nuclear emulsion detector for rapid
31 installation at multiple observation sites in the field, and installed these at 11 sites
32 around the volcano. The images in the developed emulsion films were digitized into
33 segmented tracks with a high-speed automated readout system. The muon tracks in
34 each emulsion detector were then reconstructed. After the track selection, including
35 straightness filtering, the detection efficiency of the muons was estimated. Finally, the
36 density distributions in 2D angular space were derived for each observation site by
37 using a muon flux and attenuation models.

38 The observed muon flux was compared with the expected value in the free sky, and is
39 $88\% \pm 4\%$ in the forward direction and $92\% \pm 2\%$ in the backward direction. The
40 density values were validated by comparison with the values obtained from gravity
41 measurements, and are broadly consistent, except for one site. The excess density at

42 this one site may indicate that the density inside the cone is non-axisymmetric, which
43 is consistent with a previous geological study.

44 **1 Introduction**

45 Scoria or cinder cones are a simple volcanic structure, along with stratovolcanoes,
46 shield volcanoes, and lava domes. Understanding the internal structure of scoria cones
47 is important for volcanic hazard assessments. The internal structure of scoria cones
48 has been mainly investigated by geological approaches. Kereszturi and Németh (2012)
49 presented a schematic cross-section of typical scoria cones, and Geshi and Neri (2014)
50 presented detailed photographs of the feeder dike and interior of a scoria cone formed
51 by the 1809 Etna eruption. Yamamoto (2003) investigated outcrops of the interior of
52 scoria cones in the Ojika-jima monogenetic volcano group, Nagasaki Prefecture, Japan.
53 Yamamoto (2003) classified 40 scoria cones according to their degree of interior welding
54 and proposed a link between lava outflow and cone collapse. However, scoria cones with
55 such outcrops are rare, and the internal structure can vary markedly among cones.
56 Therefore, non-destructive methods are required to investigate scoria cones that lack
57 outcrops.

58 Muography is a non-destructive technique for investigating the internal density
59 structure of large objects, employing the strong penetrating force of muons, which are
60 high-energy elementary particles contained in cosmic rays. Muography has also been
61 used for studying volcanoes, including visualization of a shallow conduit (e.g., Tanaka
62 et al., 2009), detection of temporal changes in water level due to hydrothermal activity
63 (Jourde et al., 2016), and 3D density imaging of a lava dome using a joint inversion of
64 muographic and gravity data (Nishiyama et al., 2017).

65 In unidirectional muography, the only measurable quantity is the density length,
66 which is the integral of density and length along the muon direction. It has no spatial
67 resolution along the muon path. Therefore, even if an interesting density contrast is
68 found below the crater, this could reflect contributions from other parts of the volcanic
69 body. Similar to X-ray computed tomography, which has been developed as a 3D density
70 imaging technique, muography can obtain 3D spatial resolution by increasing the
71 number of observation directions. In previous studies, muography of volcanoes has
72 been conducted in two or three directions (Tanaka et al., 2010; Rosas-Carbajal et al.,
73 2017). However, the spatial resolution is not sufficient to determine the detailed
74 structure of the volcanic interior. Nagahara and Miyamoto (2018) undertook a 3D
75 density reconstruction based on multi-directional muography and the filtered back-
76 projection technique. Their study showed that it is necessary to increase the number of
77 directions to obtain 3D spatial resolution in volcanological studies.

78 Nuclear emulsion is a type of muon detector, and has been used for studies of
79 volcanoes (Tanaka et al., 2007; Nishiyama et al., 2014; Tioukov et al., 2019). The
80 trajectories of high-energy charged particles that pass through an emulsion film are
81 recorded as aligned silver grains with micron-scale resolution (Nakamura et al., 2005;
82 Tioukov et al., 2019; Nishio et al., 2020). The positions and slopes of aligned grains in a
83 developed emulsion film are digitized with an automated emulsion readout system
84 (Kreslo et al., 2008; Morishima and Nakano, 2010; Bozza et al., 2012; Yoshimoto et al.,
85 2017). Unlike hodoscopes using scintillator bars (e.g., Saracino et al., 2017) or multi-
86 wire proportional chambers (Olah et al., 2018), a nuclear emulsion film does not have
87 temporal resolution. In contrast, an emulsion detector does not require electricity,

88 which facilitates the installation of such detectors around volcanoes where the
89 infrastructure is not well developed.

90 In muographic studies of a volcano, contamination by low-momentum particles must
91 be removed to derive the correct density (Nishiyama et al., 2014, 2016). Thus, nuclear
92 emulsion detectors have often been used as an emulsion cloud chamber (ECC), which
93 comprises alternating layers of films and lead or iron plates (e.g., Kodama et al., 2003).

94 An ECC detector can measure the momentum of the charged particles, one by one,
95 by detecting deflection angles caused by multiple Coulomb scattering (Agafonova et al.,
96 2012). For multiple Coulomb scattering, there is a relationship between the maximum
97 detectable momentum p_{max} and position resolution y_{reso} as follows using the first term
98 of Eq. (33.16), and (33.20) in Tanahashi et al., (2018):

$$p_{max} \sim \alpha X_0^{-0.5} \chi^{1.5} y_{reso}^{-1} \quad (1)$$

100 where α is a constant, X_0 is the radiation length of a material, and χ is the thickness of
101 the material. The position resolution of the newest scintillator hodoscope or MWPC is
102 on the order of 1 mm (Saracino et al., 2017; Olah et al., 2018). In the case of nuclear
103 emulsion, the resolution is about 1 μm . When using ECC, the thickness of the material
104 can be reduced to 1/100 while maintaining the same p_{max} , which is advantageous in
105 terms of transportation in the field.

106 A new design of the ECC detector was also required for its rapid installation at
107 multiple observation sites in the field. In a previous study of volcano observations
108 using the ECC detector (Nishiyama et al., 2014), rapid installation of the detector was
109 not required because the number of observation sites was just one. It is also important
110 to establish a data analysis procedure for the muon tracks recorded by the ECC
111 detectors. To derive an accurate density value for the volcanic body, it is necessary to

書式を変更: フォントの色 : 自動

書式を変更: フォントの色 : 自動

コメントの追加 [宮本 成悟2]: RC1

Lines 93-94: "An ECC detector can measure the momentum of the charged particle by detecting deflection angles caused by multiple Coulomb scattering."

In my opinion a ECC doesn't measure the momentum. It can provide a statistical information of the momentum of the muons, as correctly described in the section 4.2

書式を変更: フォントの色 : 自動

書式を変更: フォントの色 : 自動

コメントの追加 [宮本 成悟3]: RC1 : Line 97: Please describe better and/or give a reference about the formula (1)

112 remove low-momentum contamination, estimate the detection efficiency, and validate
113 the results. In addition, for bias-free 3D imaging by multi-directional muography, the
114 installed muon detectors must show similar performance.

115 **2 Izu–Omuroyama scoria cone**

116 The Izu–Omuroyama scoria cone (34°54'11"N, 139°05'40"E; 580 m a.s.l.) is one of the
117 largest scoria cones in the world, and is part of the Higashi Izu monogenetic volcano
118 group (Aramaki and Hamuro, 1977), which is located in the northeastern Izu
119 Peninsula, Ito City, Shizuoka Prefecture, Japan. It is considered to have formed about
120 4,000 years ago, based on ¹⁴C dating (Saito et al., 2003). The basal diameter is 1,000 m,
121 the height is 280 m from the base, and the typical slope of its flanks are 29–32°. The
122 center of the cone contains a crater that is 250 m wide and 40 m deep. The volume of
123 the cone is $71 \times 10^6 \text{ m}^3$, and lava with a volume of $\sim 10^8 \text{ m}^3$ has flowed out from the
124 base of the cone (Koyano et al., 1996). The lava is a basaltic andesite with 54–56 wt.%
125 SiO₂ (Hamuro, 1985).

126 Although the shape of the Izu–Omuroyama scoria cone appears to be axisymmetric
127 (Fig. 1), a geological study suggested it has an anisotropic structure due to the
128 following reasons. (i) During/after the growth of the cone, some interior parts became
129 welded due to loading, residual heat, and a low cooling rate. As a result, some denser
130 material formed. (ii) At the end of the eruption, a lava lake was formed in the crater,
131 and the lava flowed out to the western foot of the cone. (iii) There is a small crater on
132 the south side of the cone, which is thought to have formed when the main crater was
133 blocked at the end of the eruption (Koyano et al., 1996).

コメントの追加 [宮本 成悟4]: RC1, Line 117 “at 4
ka” It is not clear to me which is the age.

134 The bulk density of typical continental crust is about $2.6\text{--}2.7 \times 10^3 \text{ kg m}^{-3}$. The bulk
135 densities reported for scoria deposits are $0.84\text{--}1.01 \times 10^3 \text{ kg m}^{-3}$ (Taha and Mohamed,
136 2013) and $0.56\text{--}1.20 \times 10^3 \text{ kg m}^{-3}$ (Bush, 2001). Therefore, the maximum expected
137 density contrast is about $1.4\text{--}2.0 \times 10^3 \text{ kg m}^{-3}$, due to the difference in porosity
138 between welded rocks and scoria deposits. In addition, the Izu–Omuoyama scoria cone
139 is an ideal target for multi-directional muography due to the accessibility to detector
140 sites and absence of muographic shadows from any direction caused by other
141 topographic features.
142



143 Figure 1. Photograph of the Izu–Omuroyama scoria cone from the northwest, taken by
144 an unmanned aerial vehicle (Koyama, 2017).
145

146 **3 Multi-directional muography observations using emulsion cloud chambers**

147 **3.1 Detector design**

148 Emulsion films were manufactured by pouring 70 μm of nuclear emulsion on both
149 sides of a 180 μm -thick plastic base. The size of a film is 125×100 mm. The films were
150 vacuum-packed in a light-blocking envelope to maintain their planar form, which
151 prevented air bubbles forming between the envelope and film, and made it easy to
152 handle the films in the field.

153 The detector used for the 2018 observations is basically the same as that of Nishiyama
154 et al. (2014), and only the number of lead plates was different. The former consists of
155 20 films and 9 plates of 1-mm-thick lead, the latter consists of 20 films and 19 lead
156 plates. At the time of installation in 2018, the films, lead plates, and supports were all
157 in pieces and, therefore, a lot of time and effort was required for assembly in the field.
158 The more efficient detector design was required for rapid and error-free installation.

159 The detector used in the 2019 observations was improved. It consists of an ECC and
160 an outer box. The ECC consists of 20 emulsion films and 19 lead plates, each 1 mm
161 thick (Fig. 2a). An aluminum frame was fixed to a lead plate with a thin sheet of glue,
162 and then an emulsion film with the light-blocking envelope was attached with scotch
163 tape. In this paper, we term this unit the emulsion-lead plate (EL plate; Fig. 2a). The
164 EL plate was designed for quick assembly in the field.

165 The outer box consists of 10-mm-thick aluminum plates (Fig. 2b). The outer size of
166 this box is 190 mm in width, 155 mm in height, and 90 mm in depth. An ECC and
167 strong springs were placed in the box. There are four screw holes on one side of the box,
168 and by turning the bolts and pushing the spring plate, a uniform pressure ($\sim 10^5$ Pa)

169 was applied to the ECC. This pressure prevents the film from stretching and shrinking
170 due to temperature changes.

171 Given that there is no temporal resolution in emulsion films, ordinary ECC detectors

172 cannot distinguish whether cosmic-ray tracks pass the ECC during muographic

173 observation or transportation and standby. Thus, we also added a similar gimmick as

174 previous muographic studies using emulsion films as previous muographic studies

175 using emulsion films. The researchers have been used emulsion films with a different

176 alignment during the muon observations and standby (e.g., Tanaka et al., 2007). In the

177 present study, the corners of the EL plates were aligned during the muon observations,

178 while the corners were intentionally shifted a few millimeters horizontally and fixed

179 with clamps during standby (Fig. 3). This alignment difference distinguishes passing

180 charged particles during non-observation and observation periods by pattern matching

181 of each emulsion film. By using this procedure, the time to set the alignment between

182 each EL plate in the field is <30 s. Although the muon tracks that pass through an

183 ECC during the alignment set-up may become noise, our procedure reduced such

184 tracks.

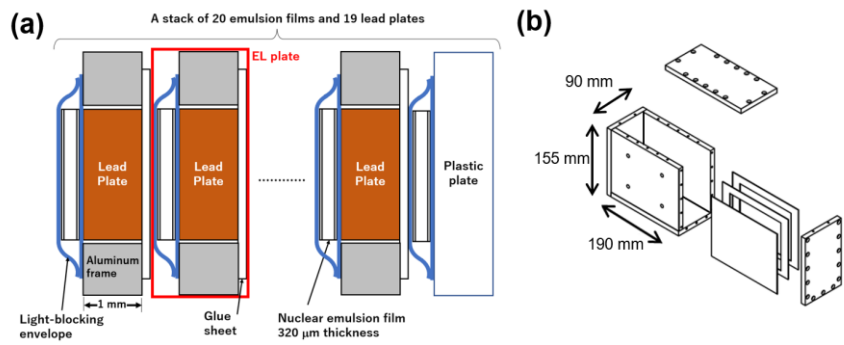
185

書式を変更: フォントの色 : 自動

書式を変更: フォントの色 : 自動

書式を変更: フォントの色 : 自動

コメントの追加 [高本 成悟5]: RC1: Lines 169-170
“we needed to add time information to the ECC” It is
not very clear the meaning of this sentence. Please
rephrase.

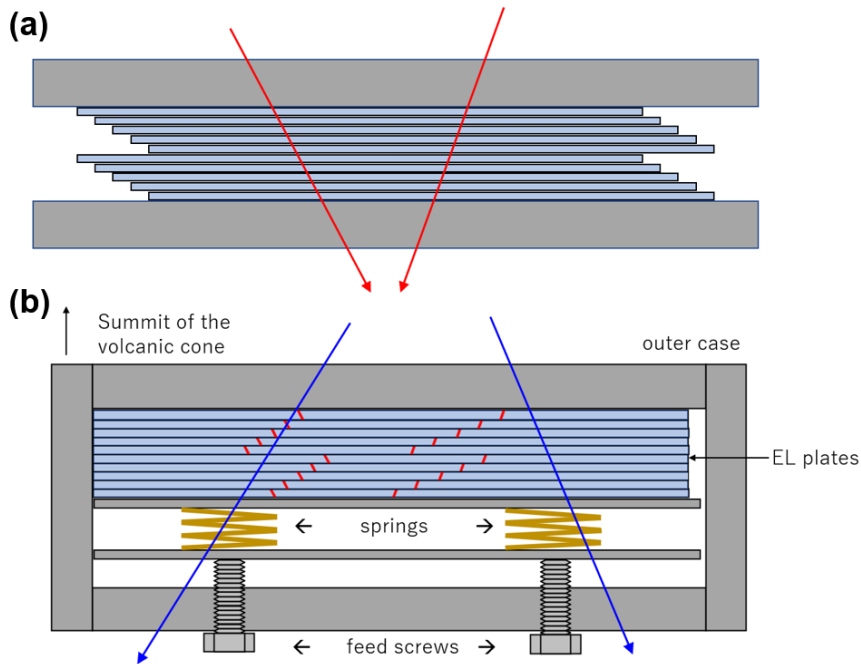


186

187 Figure 2. Design of the ECC and outer box. (a) Schematic cross-section of the EL plates
 188 and an ECC. The EL plate consists of a 1-mm-thick aluminum frame, 1-mm-thick lead
 189 plate, 100- μm -thick glue sheet that fixes a lead plate to an aluminum frame, and an
 190 emulsion film with a light-blocking envelope. An ECC consists of 19 EL plates and an
 191 emulsion film with a plastic plate. (b) Schematic of the aluminum outer box. The
 192 thickness of the aluminum plate is 10 mm. The ECC shown in (a) was set inside this
 193 box. There are four holes for feed screws in the front plate.

194

195



196

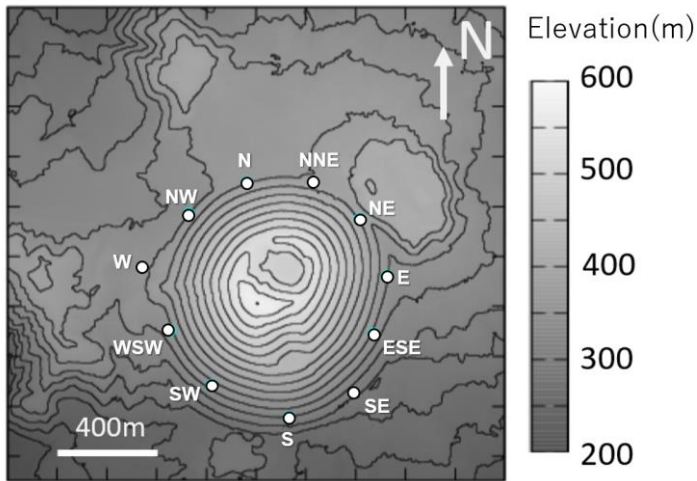
197

198 Figure 3. (a) View of the EL plates from above during standby. The EL plates were
199 intentionally shifted a few millimeters horizontally and fixed with a pair of steel plates
200 and clamp. The red lines represent the muon tracks in this alignment. (b) View from
201 above during the observations. The EL plates were aligned to the side of the outer box,
202 and fixed by the springs and feed screws. The blue lines represent muon tracks during
203 observations. Note that the red tracks cannot be reconstructed in this alignment.
204

205 **3.2 Installation**

206 The detectors were installed at three sites in 2018 and eight sites in 2019 around the
207 Izu–Omuroyama scoria cone (Fig. 4; Table 1). Each detector was buried in a hole that
208 was about 40 cm deep to avoid high temperatures due to direct sunlight. This is done
209 because the number of latent image specks decreases, and the number of randomly
210 generated specks increases, under high-temperature conditions (Nishio et al., 2020).
211

212



213

214

215 Figure 4. Topography of the Izu–Omuroyama scoria cone. White dots represent
216 observation sites.

217

Detector site ID	Effective area (cm ²)	Exposure time (days)
W, SE, and NNE (2018)	120	60
N, NW, WSW, SW, S, ESE, E, and NE (2019)	240	90

218 Table 1. Effective area and muon exposure time for each detector.

219

220

221 The installation procedure at each observation site in 2019 was as follows (Fig. 5).

- 222 1) Carry the outer box and EL plates to the observation site.
- 223 2) Measure the coordinates of the site with a hand-held GPS (GERMIN; model GPS
224 eTrex 30J). The typical uncertainty of the latitudinal and longitudinal coordinates
225 is 3 m.
- 226 3) Dig a hole in the ground with horizontal dimensions of 60 × 40 cm and a depth of
227 40 cm.
- 228 4) Flatten the base of the hole, place a plastic bag inside the hole, and lay down a
229 piece of plywood.
- 230 5) Put double-sided tape on the bottom of the outer box and place it on the plywood.
- 231 6) Put the stack of EL plates into the box and quickly align these (<30 s).
- 232 7) Close the cap of the outer box.
- 233 8) Turn the feed screws to increase the pressure.
- 234 9) Measure the attitude of the outer box (i.e., the yaw, **[absolute azimuth angle]**
235 **,** roll, and pitch). The yaw was measured with a fiber optic gyro (Japan
236 Aviation Electronics Industry Ltd.; model FOG JM7711; Watanabe et al., 2000),
237 **and, the** roll and pitch were measured by the digital leveler. The typical errors on
238 the yaw, roll, and pitch are 8.7×10^{-3} , 1.0×10^{-3} , and 1.0×10^{-3} **radians,**
239 respectively.
- 240 10) Cover with styrofoam to avoid heating from the ground surface.
- 241 11) Close the plastic bag to keep water out.
- 242 12) Backfill the hole.

243

コメントの追加 [宮本 成悟6]: RC1: Is the absolute azimuth coordinates provided directly by the instrument ?

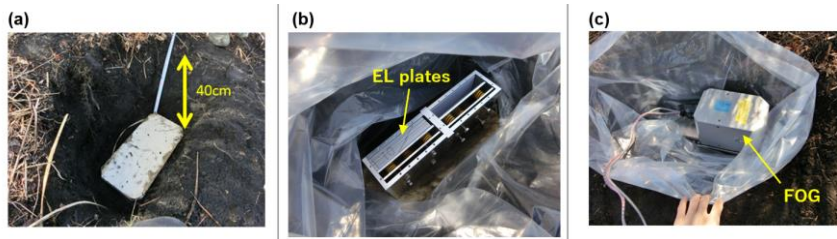
Which are the angles measured with the FOG and which with the digital leveler ?

書式を変更: フォントの色 : 自動

コメントの追加 [宮本 成悟7]: RC1: Line 232: please provide the units of the errors the angles.

244 The time taken for this installation was ~2 h for each site, and we installed detectors
245 as three sites in a day in 2019. The detector retrieval procedure was the opposite of the
246 installation procedure. The 380 films were developed in a darkroom. The deposited
247 silver particles on the surface of the films were removed with anhydrous ethanol. The
248 gelatin of the sensitive layer was swollen with a glycerin solution to obtain the
249 optimum thickness for an automated track readout system, which is described in the
250 next section.
251

252



253

254

255 Figure 5. Photographs showing the installation procedure. (a) Dig a hole and place a
256 plywood sheet in the bottom. (b) Place the outer box in the hole and put a stack of EL
257 plates into the box. The plates were aligned over a period of <30 s. After closing the top
258 plate of the box, the feed screws were tightened to increase the pressure. (c) The yaw,
259 roll, and pitch were measured with a fiber optic gyro (FOG) and digital level.

260

261 **4 Track reconstruction, selection, and detection efficiency estimation**

262 **4.1 Track reconstruction**

263 A track of a high-energy charged particle is recorded as an aligned line of silver grains
264 in the emulsion film (e.g., Nakamura et al., 2005). The images in the 380 nuclear
265 emulsion films were scanned and the positions and slopes of the tracks were digitized
266 by “HTS”, which is a high-speed automated track readout system at Nagoya University
267 (Yoshimoto et al., 2017). For each ECC, the tracks of the charged particles were
268 digitally reconstructed from the segmented tracks in 20 films. NETSCAN 2.0 software
269 was used for track reconstruction (Hamada et al., 2012). NETSCAN 2.0 rapidly
270 corrects for film distortions and local misalignments between films by using many
271 tracks recorded over a large area. It then outputs all possible connections as the final
272 result. NETSCAN 2.0 has been used in various fields, such as neutrino physics
273 (Hiramoto et al., 2020), cosmic ray astronomy (Takahashi et al., 2015), and muographic
274 studies of Egyptian pyramids (Morishima et al., 2017). The typical procedure for the
275 track reconstruction is as follows.

276

- 277 1) Reconstruct the “base track”, which is connected between the emulsion layers
278 across the plastic base of 170 μm in a film.
- 279 2) Reconstruction of the “linklet”, which is the base track pair between adjacent films
280 across lead plates.
- 281 3) Reconstruction of the tracks that connect across the whole ECC. If no base track
282 was found in two consecutive films on the extension of a track, then the track was
283 considered to have stopped.

284

285 For example, in ECC_ID = 02, 8.9×10^6 base tracks, 3.2×10^6 linklets in a pair of
286 adjacent films, and 1.7×10^7 tracks in an entire ECC were reconstructed.

コメントの追加 [宮本 成悟8]: RC1 : Lines 315-316:
how many are the candidate tracks ?

287 4.2 Track selection

288 NETSCAN 2.0 outputs all possible track connections. Therefore, it is necessary to
289 carefully select the tracks for the muographic analysis. A schematic example of the
290 output tracks is shown in Fig. 6. Most of the branches can be considered to represent
291 contamination by fake base tracks caused by random noise, or the coincidental
292 occurrence of low-energy positrons/electrons on parallel slopes in the vicinity of the real
293 tracks (e.g., Fig. 6; cases 2 and 3). [For reference, the position dependence of noise](#)
294 [density is described in Appendix A.](#) Some branches consist of a pair of straight tracks
295 with small closest distances and similar angles (Fig. 6; case 4). In this case, the two
296 tracks should be separated.

書式を変更: フォントの色 : 自動

コメントの追加 [宮本 成悟9]: for RC2

297 The following χ^2/ndf value was calculated for all tracks for the low momentum cut-
298 off:

$$299 \chi^2/ndf = \sum_m \left[\left(\frac{\Delta\theta_R^m}{\sigma_R^m} \right)^2 + \left(\frac{\Delta\theta_L^m}{\sigma_L^m} \right)^2 \right] / ndf \quad (2)$$

300 where ndf is the number of degrees of freedom and m is the index of adjacent film pairs
301 (i.e., [1,2], [2,3], [3,4], ..., and [18,19], [19,20] in Fig. 6) or with one skip if there was a
302 base track inefficiency (i.e., [1,3], [2,4], [3,5], ..., [17,19], [18,20]). $\Delta\theta_R^m =$
303 $(\Delta\theta_x^m \times \tan \theta_x + \Delta\theta_y^m \times \tan \theta_y) / \sqrt{\tan^2 \theta_x + \tan^2 \theta_y}$ and $\Delta\theta_L^m = (\Delta\theta_y^m \times \tan \theta_x -$
304 $\Delta\theta_x^m \times \tan \theta_y) / \sqrt{\tan^2 \theta_x + \tan^2 \theta_y}$, and $\Delta\theta_x^m$ and $\Delta\theta_y^m$ are angular differences along the
305 x, y coordinates of the ECC. σ_R^m and σ_L^m are the root-mean-square of $\Delta\theta_R^m$ and $\Delta\theta_L^m$,

306 which were calculated for every adjacent film pair in every ECC (Fig. 7). Figure 8
307 shows the distribution of χ^2/ndf for all tracks in an ECC.

308 The procedure for track selection is as follows.

- 309 1) Select tracks that start from one of the two most upstream (i.e., summit cone side)
310 films and stop at one of the two most downstream films.
- 311 2) Select tracks with $\chi^2/ndf < 5.0$.
- 312 3) If a track has any branches, then:
 - 313 a) If the shared proportion of track length is $\geq 20\%$, choose the longest branch. If
314 the track lengths are the same, then choose the branch with the smallest
315 χ^2/ndf .
 - 316 b) If the shared proportion of track length is $< 20\%$ (Fig. 6; case 4), then the
317 branches were divided into two tracks.

318 We estimated the effect of the straightness filtering using $\chi^2/ndf < 5.0$. Figure 9 shows
319 the momentum filtering efficiency. This figure was derived from a simple simulation in
320 which the interaction of charged particles inside the ECC was assumed to be multiple
321 Coulomb scattering only, and the scattering angle was approximated by a Gaussian
322 distribution. The path length in the lead plates becomes longer when the track has a
323 larger slope, and thus the momentum also becomes higher. Based on the background
324 noise study by Nishiyama et al. (2016), the size of the mountain body used in the
325 simulation and the Izu–Omuroyama scoria cone is broadly the same, and thus the
326 rejection efficiency should be sufficient. For example, after the track selection,
327 1.7×10^6 tracks were selected at the site “N”.

328

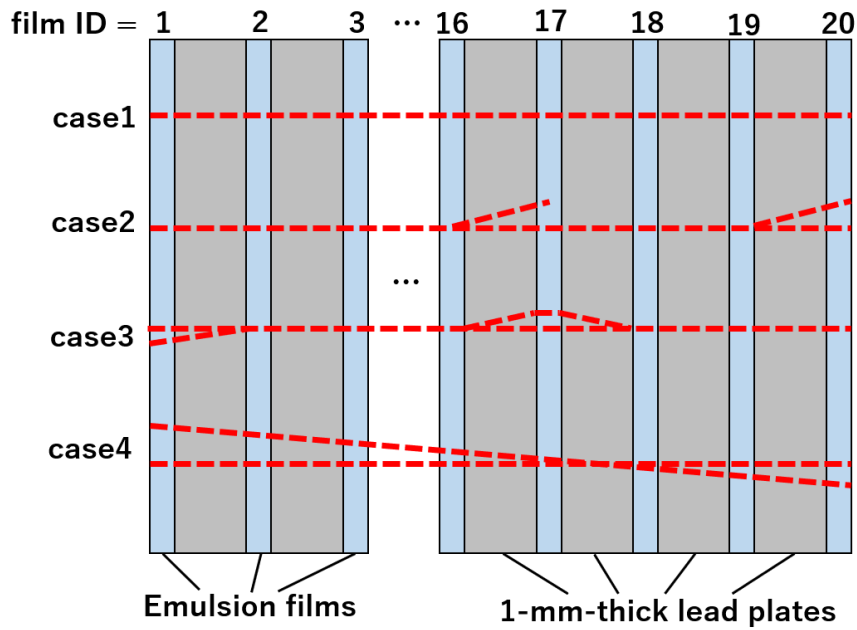
329

書式を変更: フォントの色 : 自動

コメントの追加 [宮本 成悟10]: RC1 , Lines 310-311:
How do you evaluate the filtering efficiency ? It is not described and no reference is given.

書式を変更: フォントの色 : 自動

330



331

332

333 Figure 6. Schematic examples of typical reconstructed tracks in an ECC obtained by
334 NETSCAN 2.0. Upstream means towards the volcanic cone side and downstream
335 means the backward free sky direction.

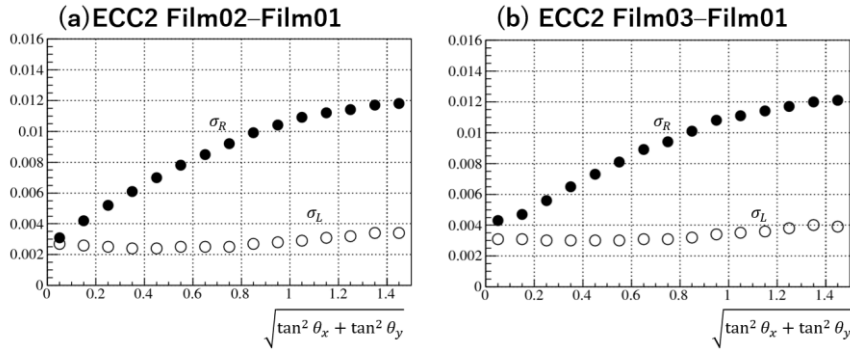
336 Case 1: a straight track without any branches.

337 Case 2: a straight track with a branch in the middle and downstream films. The track
338 branch in the middle was rejected by selection step (1). The branch in the most
339 downstream film was merged into the straight track by selection step 3a.

340 Case 3: branches in the upstream and middle films. Both branches were merged into a
341 straight track by selection step 3a.

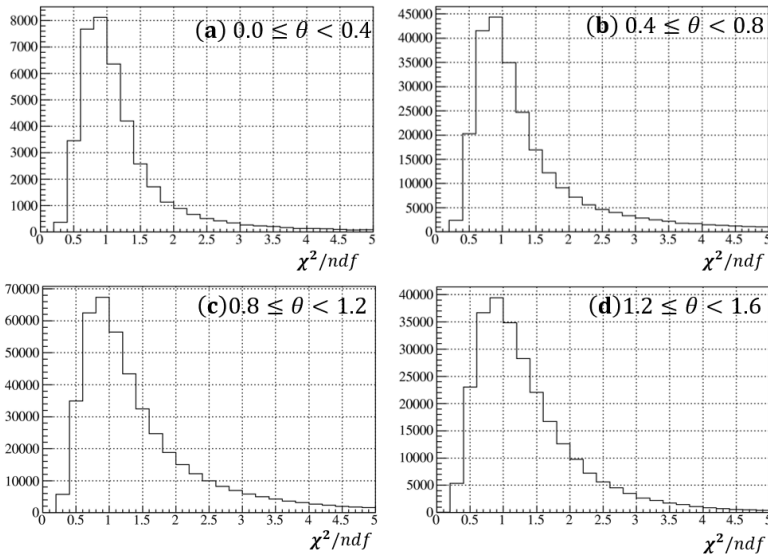
342 Case 4: a pair of straight tracks with small closest distances and similar angles. If the

343 shared proportion of the track length was <20%, the tracks were divided into two
344 different tracks by selection step 3b.
345

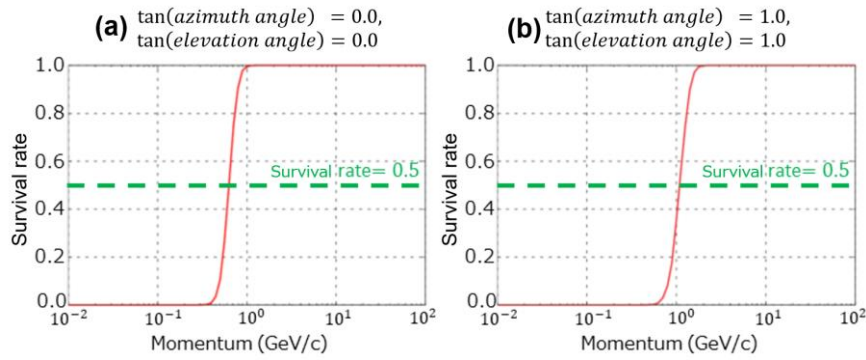


346
 347 Figure 7. Examples of σ_R and σ_L as a function of $\sqrt{\tan^2 \theta_x + \tan^2 \theta_y}$. The values were
 348 determined by the ECC and used to calculate the value of Eq. (2).

349



350
 351 Figure 8. Example of the χ^2/ndf distribution for selected tracks as a function of $\theta =$
 352 $\sqrt{\tan^2 \theta_x + \tan^2 \theta_y}$ in an ECC. (a) $0 \leq \theta < 0.4$, (b) $0.4 \leq \theta < 0.8$, (c) $0.8 \leq \theta < 1.2$, and (d)
 353 $1.2 \leq \theta < 1.6$.



354

355 Figure 9. Survival rate of muons after the straightness cut-off as a function of

356 momentum. (a) Track angles with $\tan(\text{relative azimuth}) = 0.0$ and

357 $\tan(\text{elevation angle}) = 0.0$. (b) Track angles with $\tan(\text{relative azimuth}) = 1.0$ and

358 $\tan(\text{elevation angle}) = 1.0$. The path length in the lead plates becomes longer when the

359 track has a larger slope, and thus the remaining momentum also becomes higher for

360 the latter case. The momentum values at a survival rate of 0.5 are 0.6 and 1.1 GeV/c,

361 respectively.

362

363 **4.3 Detection efficiency estimation**

364 The muon detection efficiency can be estimated by investigating the percentage of
365 tracks that have a base track in a film. In this paper, we term this percentage the “fill
366 factor”. The fill factor ε can be defined as follows:

367
$$\varepsilon_j(\theta_x, \theta_y) = \frac{N_j(\theta_x, \theta_y)}{N_{j-1, j+1}(\theta_x, \theta_y)} \quad (3)$$

368 where j is a film ID, $N_{j-1, j+1}(\theta_x, \theta_y)$ is the number of tracks in which base tracks were
369 found in films $j-1$ and $j+1$, and $N_j(\theta_x, \theta_y)$ is the number of tracks in which base
370 tracks were found in films $j-1, j$, and $j+1$. The fill factor depends on the films and
371 track slopes θ_x and θ_y . The position dependence of the fill factor is described in

372 Appendix A.

373 Using the fill factor $\varepsilon_j(\theta_x, \theta_y)$ and $\bar{\varepsilon}_j(\theta_x, \theta_y) = 1 - \varepsilon_j(\theta_x, \theta_y)$, the muon detection
374 efficiency ϵ in an ECC can be calculated as follows:

375
$$\epsilon(\theta_x, \theta_y) = \sum_{hit\ pattern} \varepsilon_1 \times \bar{\varepsilon}_2 \times \varepsilon_3 \times \dots \times \bar{\varepsilon}_{18} \times \varepsilon_{19} \times \varepsilon_{20} \quad (4)$$

376 where *hit pattern* is the summation for all possible hit patterns (e.g., $\varepsilon_1 \times \bar{\varepsilon}_2 \times \varepsilon_3 \times$
377 $\dots \times \bar{\varepsilon}_{18} \times \varepsilon_{19} \times \varepsilon_{20}$ or $\bar{\varepsilon}_1 \times \varepsilon_2 \times \varepsilon_3 \times \dots \times \varepsilon_{18} \times \bar{\varepsilon}_{19} \times \varepsilon_{20}$) from the track selection
378 conditions described in section 4.2 (Fig. 10). An example of the angular distribution of
379 the fill factor $\varepsilon_j(\theta_x, \theta_y)$ and muon detection efficiency $\epsilon(\theta_x, \theta_y)$ in an ECC is shown in
380 Fig. 11. The statistics of observed muons were limited in some angular bins by the
381 thick volcanic cone. However, the statistics were sufficient in the backward region (i.e.,
382 elevation angle < 0.0). We used the distribution of the negative elevation angular
383 region instead of the positive region, because it has enough statistics and the optics of
384 the HTS has an approximately two-fold rotational symmetry.

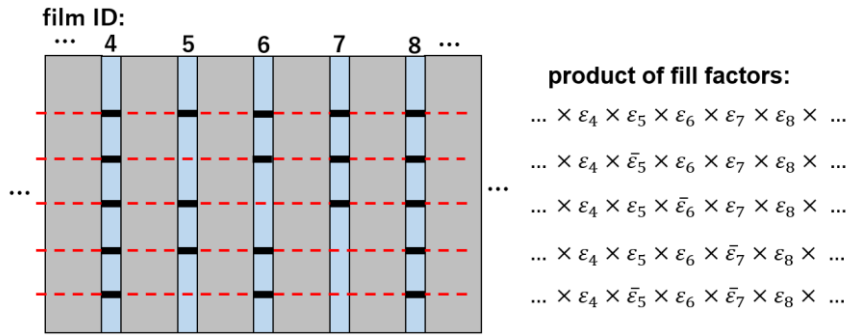
385

書式を変更: フォントの色 : 自動

コメントの追加 [宮本 成悟11]: for RC2

386

387

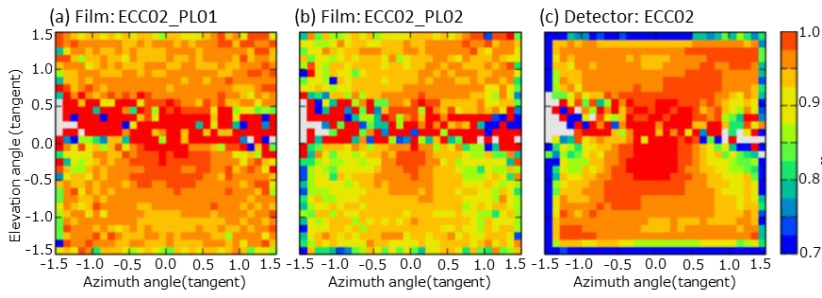


388

389 Figure 10. Example of all hit patterns and the products of fill factors in Eq. (4) when
 390 base tracks are found in film ID numbers 4 and 8. The red lines indicate the
 391 reconstructed tracks and the short black lines represent the base tracks found in the
 392 films.

393

394



395

396 Figure 11. Examples of the angular distribution of the fill factor in some films and the
397 efficiency of an ECC. (a) Fill factor for film ID = PL01 (most upstream film) and ECC
398 ID = 02 at site “N”. (b) Fill factor for film ID = PL02 and ECC ID = 02. (c) Muon
399 detection efficiency for ECC ID = 02 as evaluated by Eq. (4). The horizontal axis is the
400 tangent of azimuth angle; the vertical axis is the tangent of the elevation angle; the
401 colors represent the fill factor/efficiency values. A positive elevation angle means the
402 muon path is from the cone; a negative elevation angle means the muon path is from
403 the backward free sky. The gray color means there were no observed muons in the
404 angular bin due to the thick volcanic cone.

405

406 **5 Results**

407 The average density along muon path was determined for each observation site. We
408 used the muon flux model of Honda et al. (2004), energy loss model of Groom et al.
409 (2001), and topography around the Izu–Omuroyama scoria cone from the Geospatial
410 Information Authority of Japan (<https://maps.gsi.go.jp/>). The coordinates of the
411 observation site, direction, sensitive area, thickness of the ECC detectors, and
412 observation time were used to calculate the expected number of muons at each
413 observation site. The expected number of muons can be calculated as a function of the
414 average density ρ_k along the path:

415
$$N_k^{simu}(\rho_k) = f_k(\rho_k, L_k) \times S_k \times \Omega_k \times T \times \epsilon_k \quad (5)$$

416 where k is the index of an angular bin, $f_k(\rho_k, L_k)$ is the penetrating muon flux
417 (calculated from the muon flux model, energy loss model, and path length L_k), S_k is the
418 sensitive area of the ECC, Ω_k is the solid angle, ϵ_k is the muon detection efficiency, and
419 T is the observation time.

420 The angular bin size used for calculating the expected value was $(0.01)^2$ in terms of
421 the tangent. The angular bins were then merged to improve the statistical accuracy of
422 the observed values. This merging procedure is useful in topology where a small
423 change in elevation angle can dramatically change the path length in the volcano. If k
424 is the index of the angular bins of $(0.01)^2$ and the bins belong to a larger angular bin i ,
425 then the following equation holds:

426
$$N_i^{merged}(\rho_i) = \sum_k N_k^{simu}(\rho_i) \quad (6)$$

427 where ρ_i is the density of the merged angular bin i . If N_i^{obs} is the number of the
428 detected muons in the angular bin i , then we can uniquely determine the density value

429 ρ_i , such that $N_i^{merged}(\rho_i) = N_i^{obs}$. The lower limit ρ_i^{low} and upper limit ρ_i^{up} caused by the
430 statistical error on N_i^{obs} can also be estimated as follows:

431
$$N_i^{merged}(\rho_i^{low}) = N_i^{obs} + \sqrt{N_i^{obs}} \quad (7)$$

432
$$N_i^{merged}(\rho_i^{up}) = N_i^{obs} - \sqrt{N_i^{obs}} \quad (8)$$

433 An example of the derived density map is shown in Fig. 12. All results are shown in

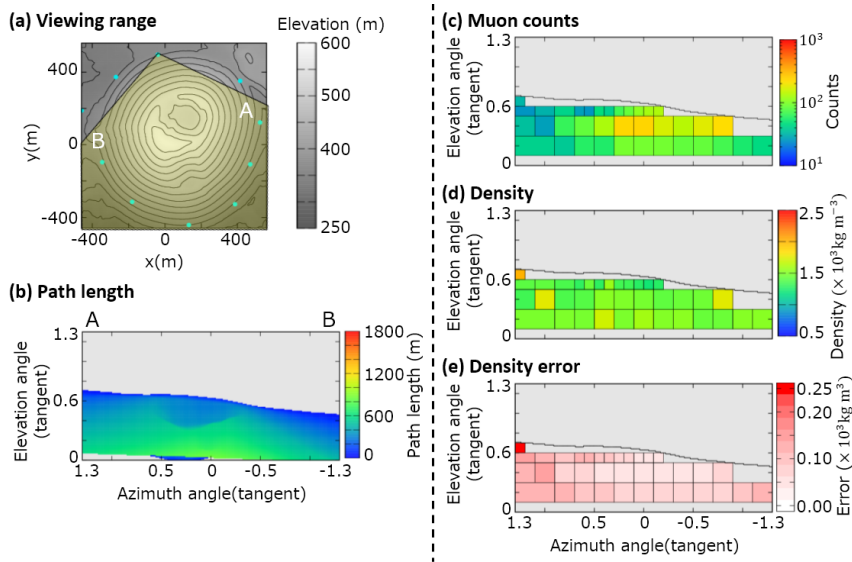
434 Figs. 17-26 (Appendix B).

435 The definition of the angular bin areas was based on the following. The size of the
436 angular bins was $(0.2)^2$ when the elevation angle is 0.1 to 0.5 in tangent terms. When
437 the elevation angle is >0.5 , the angular bin size was $(0.1)^2$. If the observed muon count
438 in the bin was <25 , the angular bin was manually merged with adjacent bins to
439 improve the statistical error. The angular bin with a near-surface path (path length $<$
440 30 m) was excluded to avoid ambiguity between the actual topography and digital
441 elevation map. The attitude errors of each muon detector also contribute to the path
442 length ambiguity, especially near the surface of the cone.

443

書式を変更: フォントの色 : 自動

444



445

446

447 Figure 12. Data for observation site N. (a) Map, topography, and viewing range; (b)
 448 path length of the volcanic cone; (c) muon counts N_i^{obs} ; (d) density ρ_i . The maximum
 449 value of the color bar indicates a density of $>2.5 \times 10^3 \text{ kg m}^{-3}$ and the minimum value
 450 is $<0.5 \times 10^3 \text{ kg m}^{-3}$. (e) Density error $\Delta\rho = (\rho_i^{up} - \rho_i^{low})/2$. The maximum value of the
 451 color bar indicates a density error of $>0.25 \times 10^3 \text{ kg m}^{-3}$.

452

453 **6 Validation**

454 Firstly, we validated the observed muon flux by comparing it with the muon flux
455 model in the free sky region. The average and standard deviation of the ratio between
456 the sites were $88\% \pm 4\%$ in the forward direction and $92\% \pm 2\%$ in the backward
457 direction, except for the NNE site (Fig. 13). An example of observed/expected muon flux
458 ratio angular distribution of the site N is shown in Fig. 14. As can be seen in this
459 figure, in each detector site, the ununiform distribution of the observed/expected muon
460 flux ratio exists. Such deviations were 4%–7% except the forward directions at the site
461 SE and NNE.

462 For reference, a 10% error on the flux
463 corresponds to a 4% error on the density length at a $\tan(\text{elevation angle}) = 0.2$ and
464 density length = 1000 m (water equivalent). These deviations were less than the errors
465 caused by the muon statistics. The discrepancy for the NNE site is discussed in the
466 next section.

467 Secondly, we compared the density of the entire volcanic cone determined by gravity
468 data with that obtained by muography. Table 2 shows the density determined from
469 each observation site when the cone is assumed to be uniform. The
470 calculation of the overall density $\bar{\rho}$ is as follows:

471
$$\bar{\rho} = \frac{\sum_i \rho_i V_i}{\sum_i V_i} \quad (9)$$

472 where i is the index of the angular bins and V_i is the volume of the volcanic cone cut off
473 by the angle bin i . Based on the gravity study of Nishiyama et al. (2021), the density of
474 the Izu–Omuroyama scoria cone is $1.39 \pm 0.07 \times 10^3 \text{ kg m}^{-3}$. The overall density
475 derived by muography at each observation site is $1.42\text{--}1.53 \times 10^3 \text{ kg m}^{-3}$, except for

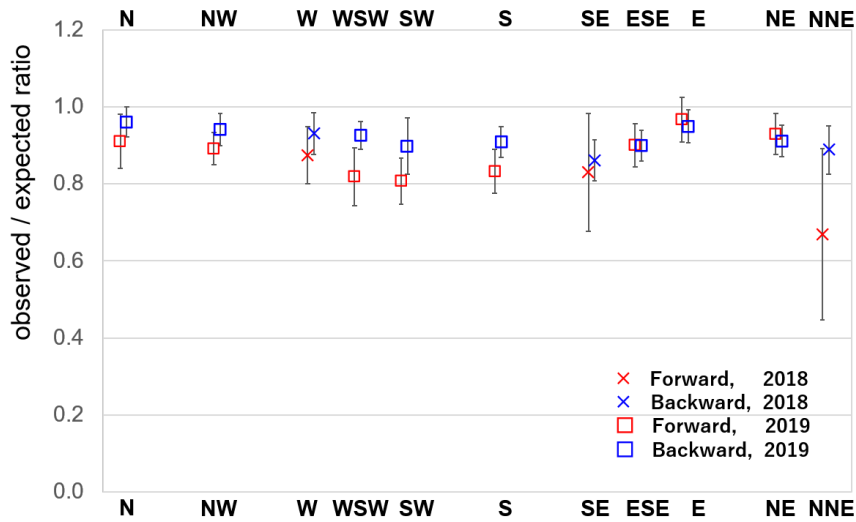
書式を変更: フォントの色 : 自動

コメントの追加 [宮本 成悟12]: RC1 : Lines 444-445:

“There were also 4%–7% in each detector site except the forward directions at the SE and NNE site “

This sentence is not clear to me.

476 one site. These values are broadly consistent with the density determined from gravity
477 data, except for the observation site W ($1.72 \times 10^3 \text{ kg m}^{-3}$).

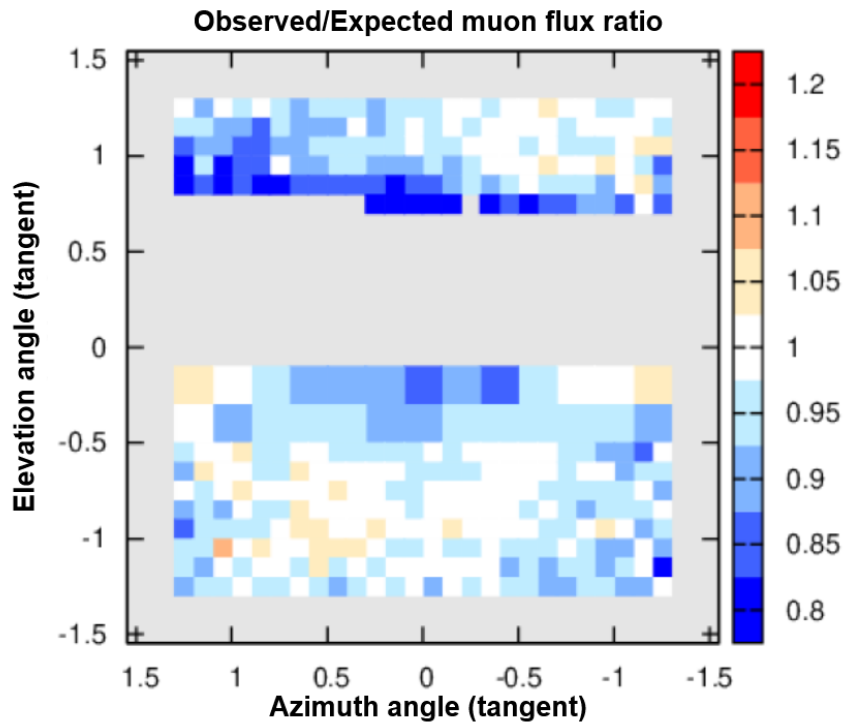


478

479 Figure 13. The observed/expected muon flux ratio for each observation site in the
 480 free sky region. The plot represents the average value of the ratio in tangential
 481 angular space, and the error bars are the standard deviations at each site.

482

483



484

485

486 Figure 14. Example of the observed/expected muon flux ratio in the free sky region at
487 site N. The horizontal axis represents azimuth angle, and the vertical axis represents
488 the elevation angle. Positive elevation angle means the muons come from forward
489 directions (the volcanic cone). Negative elevation angle means the muons come from
490 backward free sky directions. Typical deviation of the ratio is 4%–7% in each site.

491

492

493

Observation site	Overall density $\bar{\rho}$ ($\times 10^3$ kg m $^{-3}$)	Observation site	Overall density $\bar{\rho}$ ($\times 10^3$ kg m $^{-3}$)
N	1.51	S	1.49
NW	1.45	ESE	1.45
W	1.72	E	1.42
WSW	1.50	NE	1.53
SE	1.46	NNE	1.50
SW	1.48		

494 Table 2. Overall bulk density obtained by muography, assuming that the density is

495 uniform in the volcanic cone.

496

497 **7 Discussion**

498 For the observed/expected muon flux ratio in the free sky region, the values in the
499 forward direction are less than in the backward direction at many observation sites.

500 This could be because the detectors were buried in holes on steep slopes ($\sim 30^\circ$), and our
501 analysis might not account for that effect. Due to the steep slope, muons arriving from
502 the forward direction need to penetrate some amount of soil, whereas muons from the
503 backward direction can enter the detector without being affected by the soil cover. In
504 addition, the resolution of the detector coordinates is ~ 3 m, which might also contribute
505 to the discrepancy.

506 Some density results from near the ground surface are complex. Some regions near the
507 path length of 30 m appear to have relatively higher or lower density than the other
508 data (e.g., Fig. [22](#), [25](#)). One possible reason for this is the error on the detector
509 attitude. Near the surface of the volcanic cone, the difference between the calculated
510 and actual path lengths may become larger due to the error on the detector attitude.

511 The anomalous data for the NNE site also warrants further consideration. The reason
512 for this might be a difference between the digital elevation map and actual topography.
513 There is a stone wall in front of the buried detector at this site, which is about 1 m high
514 and located on the volcanic cone side. The grid size of the digital elevation map used in
515 this study is 1 m, and thus the map might not record this steep gradient.

516 In summary, errors in the position and attitude of the detectors, and the accuracy of
517 the DEM, might cause a misfit between the DEM and actual topography. These are the
518 main reasons for the discrepancy between the observed and expected muon flux.

519 The discrepancy between the observed and expected muon flux was $\pm 4\%$ in the
520 forward direction and $\pm 2\%$ in the backward direction between the detectors. In

521 addition, the typical deviation inside each site was 4%–7%. These values are smaller
522 than the statistical error of the observed muons used to determine the density of the
523 volcanic cone, and thus they were not significant for our observations. It is interesting
524 to consider if an improvement in the accuracy of the detector position and attitude, and
525 the DEM, would decrease this systematic error. For example, the $\pm 4\%$ deviation in the
526 forward direction would be expected to decrease to $\pm 2\%$, because the misfit effect is
527 less in the backward direction. Further improvements will require simulation of the
528 expected muon flux that take into account more processes and verification of the
529 systematic errors associated with the ECC detectors.

530 The obtained density values ($1.42\text{--}1.53 \times 10^3 \text{ kg m}^{-3}$; this study) and 1.39 ± 0.07
531 $\times 10^3 \text{ kg m}^{-3}$ (Nishiyama et al., 2021) for Izu–Omuroyama scoria cone are broadly
532 consistent (Table 2). In a previous study, Rosas-Carbajal et al. (2017) identified an
533 offset between the density obtained by muon and gravity data and the density obtained
534 from muon data was $0.5 \times 10^3 \text{ kg m}^{-3}$ less than that obtained from gravity data. In our
535 validation, this discrepancy does not exist. As Rosas-Carbajal et al (2017) suggested,
536 the discrepancy might be due to differences in the filtering performance for low-
537 momentum particles shown in Fig. 9.

538 The higher density obtained at site W cannot be explained by the systematic errors
539 described above. One possible reason for this is an actual high-density structure in
540 front of the site. This hypothesis is consistent with the fact that lava flowed out from
541 the crater lake to the west (Koyano et al., 1996).

542

543 **8 Conclusions**

544 A muographic study of the Izu–Omuroyama scoria cone was undertaken in 11
545 directions. The ECC detector design was optimized for quick installation in the field.
546 We mounted the 11 detectors beneath the ground, surrounding the volcanic cone. The
547 tracks of charged particles that passed through the ECCs were reconstructed using the
548 automated emulsion track readout system HTS and NETSCAN 2.0 software. After
549 track selection, including momentum filtering and efficiency estimation, the density
550 profiles in 2D angular space were derived for each observation site. The methods
551 described in this paper can be applied to the observation of other volcanoes and target
552 objects.

553 We compared the observed muon flux to the expected value from a muon flux model in
554 the free sky region. The muon flux difference between each detector was 4% in the
555 forward directions and 2% in the backward directions, and the typical deviations in
556 each site were about 4%–7%. The errors on the detector coordinates and attitude, and
557 DEM, are the main cause of the discrepancy between the observed and expected muon
558 flux.

559 In addition, we also compared our results with the overall volcanic cone density
560 estimated from gravity data, which are broadly consistent, apart from the W site. This
561 discrepancy for the W site can be explained by the systematic errors discussed in the
562 previous section and statistical error of the observed muons. It might also reflect a
563 high-density structure located in the western flank of the volcano. Further 3D density
564 reconstructions of the Izu–Omuroyama scoria cone are ongoing using the data set
565 described in this paper.

566

567 **Acknowledgements**

568 The authors thank Hideaki Aoki and his colleagues of Ike-kankou for collaborating on
569 our study. We also thank Masakazu Ichikawa of the Earthquake Research Institute,
570 the University of Tokyo, for support during the observation campaign. We are also
571 grateful for the technical support of the staff and students in F-lab, Nagoya University,
572 especially with the nuclear emulsion films. This research was supported by JSPS
573 KAKENHI Grant 19H01988, an Izu Peninsula Geopark Academic Research Grant
574 (2018), the Joint Research Program of the Institute of Materials and Systems for
575 Sustainability at Nagoya University (2017–2021), and a JSPS Fellowship (Nagahara;
576 Grant DC2, 19J13805).

577

578 **References**

- 579 Agafonova, N., Aleksandrov, A., Altinok, O., Anokhina, A., Aoki, S., Ariga, A., Ariga, T.,
580 Autiero, D., Badertscher, A., Bagulya, A., Ben Dhahbi, A., Bertolin, A., Besnier, M.,
581 Bozza, C., Brugière, T., Brugnera, R., Brunet, F., Brunetti, G., Buontempo, S., Cazes,
582 A., Chaussard, L., Chernyavskiy, M., Chiarella, V., Chukanov, A., D'Ambrosio, N., Dal
583 Corso, F., De Lellis, G., del Amo Sanchez, P., Déclais, Y., De Serio, M., Di Capua, F., Di
584 Crescenzo, A., Di Ferdinando, D., Di Marco, N., Dmitrievski, S., Dracos, M.,
585 Duchesneau, D., Dusini, S., Dzhatdoev, T., Ebert, J., Egorov, O., Enikeev, R., Ereditato,
586 A., Esposito, L. S., Favier, J., Ferber, T., Fini, R. A., Frekers, D., Fukuda, T.,
587 Garfagnini, A., Giacomelli, G., Giorgini, M., Göllnitz, C., Goldberg, J., Golubkov, D.,
588 Goncharova, L., Gornushkin, Y., Grella, G., Grianti, F., Guler, A. M., Gustavino, C.,
589 Hagner, C., Hamada, K., Hara, T., Hierholzer, M., Hollnagel, A., Hoshino, K., Ieva, M.,
590 Ishida, H., Jakovcic, K., Jollet, C., Juget, F., Kamiscioglu, M., Kazuyama, K., Kim, S.
591 H., Kimura, M., Kitagawa, N., Klicek, B., Knuesel, J., Kodama, K., Komatsu, M., Kose,
592 U., Kreslo, I., Kubota, H., Lazzaro, C., Lenkeit, J., Lippi, I., Ljubicic, A., Longhin, A.,
593 Loverre, P., Lutter, G., Malgin, A., Mandrioli, G., Manai, K., Marteau, J., Matsuo, T.,
594 Matveev, V., Mauri, N., Medinaceli, E., Meisel, F., Mereaglia, A., Migliozzi, P.,
595 Mikado, S., Miyamoto, S., Monacelli, P., Morishima, K., Moser, U., Muciaccia, M. T.,
596 Naganawa, N., Naka, T., Nakamura, M., Nakano, T., Naumov, D., Nikitina, V., Niwa,
597 K., Nonoyama, Y., Ogawa, S., Okateva, N., Olshevskiy, A., Paniccia, M., Paoloni, A.,
598 Park, B. D., Park, I. G., Pastore, A., Patrizii, L., Pennacchio, E., Pessard, H., Pretzl, K.,
599 Pilipenko, V., Pistillo, C., Polukhina, N., Pozzato, M., Pupilli, F., Rescigno, R.,
600 Roganova, T., Rokujo, H., Romano, G., Rosa, G., Rostovtseva, I., Rubbia, A., Russo, A.,
601 Ryasny, V., Ryazhskaya, O., Sato, O., Sato, Y., Schembri, A., Schmidt-Parzefall, W.,

602 Schroeder, H., Scotto Lavina, L., Sheshukov, A., Shibuya, H., Shoziyoev, G., Simone, S.,
603 Sioli, M., Sirignano, C., Sirri, G., Song, J. S., Spinetti, M., Stanco, L., Starkov, N.,
604 Stipcevic, M., Strauss, T., Strolin, P., Takahashi, S., Tenti, M., Terranova, F., Tezuka,
605 I., Tioukov, V., Tolun, P., Trabelsi, A., Tran, T., Tufanli, S., Vilain, P., Vladimirov, M.,
606 Votano, L., Vuilleumier, J. L., Wilquet, G., Wonsak, B., Yakushev, V., Yoon, C. S.,
607 Yoshioka, T., Yoshida, J., Zaitsev, Y., Zemskova, S., Zghiche, A., and Zimmermann, R.:
608 Momentum measurement by the multiple Coulomb scattering method in the OPERA
609 lead-emulsion target, *New J. Phys.*, 14, 013026, [https://doi.org/10.1088/1367-](https://doi.org/10.1088/1367-2630/14/1/013026)
610 [2630/14/1/013026](https://doi.org/10.1088/1367-2630/14/1/013026), 2012.
611
612 Aramaki, S., and Hamuro, K.: Geology of the Higasi-Izu monogenetic volcano group,
613 *Bull. Earthq. Res. Inst. Univ. Tokyo*, 52, 235–278, [https://repository.dl.itc.u-](https://repository.dl.itc.u-tokyo.ac.jp/record/33207/files/ji0522010.pdf)
614 [tokyo.ac.jp/record/33207/files/ji0522010.pdf](https://repository.dl.itc.u-tokyo.ac.jp/record/33207/files/ji0522010.pdf), 1977. (in Japanese)
615
616 Bozza, C., D'Ambrosio, N., De Lellis, G., De Serio, M., Di Capua, F., Di Crescenzo, A.,
617 Di Ferdinando, D., Di Marco, N., Esposito, L. S., Rosa Anna Fini, R. A., Giacomelli, G.,
618 Grella, G., Ieva, M., Kose, U., Longhin, A., Mauri, N., Medinaceli, E., Monacelli, P.,
619 Muciaccia, M. T., Pastore, A., Patrizii, L., Pozzato, M., Pupilli, F., Rescigno, R.,
620 Romano, G., Rosa, G., Ruggieri, A., Russo, A., Simone, S., Sirignano, C., Sirri, G.,
621 Stellacci, S. M., Tenti, M., Tioukov, V., Togo, V., and Valieri, C.: An integrated system
622 for large scale scanning of nuclear emulsions, *Nucl. Instrum. Methods Phys. Res. A*,
623 703, 1, 204–212, <https://doi.org/10.1016/j.nima.2012.11.099>, 2012.
624
625 Bush, A. L.: Construction Materials: Lightweight Aggregates, in “Encyclopedia of

626 Materials: Science and Technology”, Elsevier, pp 1550–1558, <https://doi.org/10.1016/B0->
627 [08-043152-6/00277-1](https://doi.org/10.1016/B0-08-043152-6/00277-1), 2001.

628

629 Geshi, N., and Neri, M.: Dynamic feeder dyke systems in basaltic volcanoes: the
630 exceptional example of the 1809 Etna eruption (Italy), *Front. Earth Sci.*, 2, 13,
631 <https://doi.org/10.3389/feart.2014.00013>, 2014.

632

633 Groom, D. E., Mokhov, N. V., and Striganov, S. I.: Muon stopping power and range
634 tables 10 MeV–100 TeV, *At. Data Nucl. Data Tables*, 78, 183–356,
635 <https://doi.org/10.1006/adnd.2001.0861>, 2001.

636

637 Hamada, K., Fukuda, T., Ishiguro, K., Kitagawa, N., Kodama, K., Komatsu, M.,
638 Morishima, K., Nakano, T., Nakatsuka, Y., Nonoyama, Y., Sato, O., and Yoshida, J.:
639 Comprehensive track reconstruction tool “NETSCAN 2.0” for the analysis of the
640 OPERA Emulsion Cloud Chamber, *J. Instrum.*, 7, P07001, <https://doi.org/10.1088/1748->
641 [0221/7/07/P07001](https://doi.org/10.1088/1748-0221/7/07/P07001), 2012.

642

643 Hamuro, K.: Petrology of the Higashi–Izu monogenetic volcano group, *Bull. Earthq.*
644 *Res. Inst. Univ. Tokyo*, 60, 335–400, [https://repository.dl.itc.u-](https://repository.dl.itc.u-tokyo.ac.jp/record/32886/files/ji0603001.pdf)
645 [tokyo.ac.jp/record/32886/files/ji0603001.pdf](https://repository.dl.itc.u-tokyo.ac.jp/record/32886/files/ji0603001.pdf), 1985.

646

647 Hiramoto, A., Suzuki, Y., Ali, A., Aoki, S., Berns, L., Fukuda, T., Hanaoka, Y., Hayato,
648 Y., Ichikawa, A. K., Kawahara, H., Kikawa, T., Koga, T., Komatani, R., Komatsu, M.,
649 Kosakai, Y., Matsuo, T., Mikado, S., Minamino, A., Mizuno, K., Morimoto, Y.,

650 Morishima, K., Naganawa, N., Naiki, M., Nakamura, M., Nakamura, Y., Nakano, N.,
651 Nakano, T., Nakaya, T., Nishio, A., Odagawa, T., Ogawa, S., Oshima, H., Rokujo, H.,
652 Sanjana, I., Sato, O., Shibuya, H., Sugimura, K., Suzui, L., Takagi, H., Takao, T.,
653 Tanihara, Y., Yasutome, K., and Yokoyama, M. (NINJA Collaboration): First
654 measurement of $\bar{\nu}_\mu$ and ν_μ charged-current inclusive interactions on water using a
655 nuclear emulsion detector, *Phys. Rev. D*, 102, 072006,
656 <https://doi.org/10.1103/PhysRevD.102.072006>, 2020.
657
658 Honda, M., Kajita, T., Kasahara, K., and Midorikawa, S.: New calculation of the
659 atmospheric neutrino flux in a three-dimensional scheme, *Phys. Rev. D*, 70, 043008,
660 <https://doi.org/10.1103/PhysRevD.70.043008>, 2004.
661
662 Jourde, K., Gibert, D., and Marteau, J.: Improvement of density models of geological
663 structures by fusion of gravity data and cosmic muon radiographies, *Geosci. Instrum.*
664 *Methods Data Syst.*, 4, 177–188, <https://doi.org/10.5194/gi-4-177-2015>, 2015.
665
666 Jourde, K., Gibert, D., Marteau, J., d'Ars, J.B., and Komorowski, J.C.: Muon dynamic
667 radiography of density changes induced by hydrothermal activity at the La Soufrière of
668 Guadeloupe volcano, *Sci. Rep.*, 6, 33406, <https://doi.org/10.1038/srep33406>, 2016.
669
670 Kereszturi, G., and Németh, K.: Monogenetic Basaltic Volcanoes: Genetic
671 Classification, Growth, Geomorphology and Degradation, *Updates in Volcanology—*
672 *New Advances in Understanding Volcanic Systems*, Karoly Nemeth, IntechOpen., DOI:
673 10.5772/51387, 2012.

674

675 Kodama, K., Hoshino, K., Komatsu, M., Miyanishi, M., Nakamura, M., Nakamura, T.,
676 Nakano, T., Narita, K., Niwa, K., Nonaka, N., Sato, O., Toshito, T., and Uetake, T.:
677 Study of electron identification in a few GeV region by an emulsion cloud chamber,
678 *Rev. Sci. Instrum.*, 74, 53, <https://doi.org/10.1063/1.1529300>, 2003.

679

680 Koyama, M.: Photographs of the Izu-peninsula by UAV, Iwanami Science Library 268,
681 Iwanami Shoten, Publishers, Tokyo, 159 pp, ISBN 9784000296687, 2017. (in Japanese)

682

683 Koyano, Y., Hayakawa, Y., and Machida, H.: The eruption of Omuroyama in the
684 Higashi Izu monogenetic volcano field, *J Geog. (Chigaku Zasshi)*, 105, 4, 475–484,
685 <https://doi.org/10.5026/jgeography.105.4.475>, 1996. (in Japanese)

686

687 Kreslo, I., Cozzi, M., Ereditato, A., Hess, M., Knuesel, J., Laktineh, I., Messina, M.,
688 Moser, U., Pistillo, C., and Pretzl, K.: High-speed analysis of nuclear emulsion films
689 with the use of dry objective lenses, *J. Instrum.*, 3, P04006,
690 <https://dx.doi.org/10.1088/1748-0221/3/04/P04006>, 2008.

691

692 Morishima, K., and Nakano, T.: Development of a new automatic nuclear emulsion
693 scanning system, S-UTS, with continuous 3D tomographic image read-out, *J. Instrum.*,
694 5, P04011, <http://dx.doi.org/10.1088/1748-0221/5/04/P04011>, 2010.

695

696 Morishima, K., Kuno, M., Nishio, A., Kitagawa, N., Manabe, Y., Moto, M., Takasaki, F.,
697 Fujii, H., Satoh, K., Kodama, H., Hayashi, K., Odaka, S., Procureur, S., Attie, D.,

698 Bouteille, S., Calvet, D., Filosa, C., Magnier, P., Mandjavidze, I., Riallot, M., Marini, B.,
699 Gable, P., Date, Y., Sugiura, M., Elshayeb, Y., Elnady, T., Ezzy, M., Guerriero, E.,
700 Steiger, V., Serikoff, N., Mouret, J., Charles, B., Helal, H., and Tayoubi, M.: Discovery
701 of a big void in Khufu's Pyramid by observation of cosmic-ray muons, *Nature*, 552, 387,
702 <https://doi.org/10.1038/nature24647>, 2017.
703
704 Nagahara, S., and Miyamoto, S.: Feasibility of three-dimensional density tomography
705 using dozens of muon radiographies and filtered back projection for volcanoes, *Geosci.*
706 *Instrum. Methods Data Syst.*, 7, 307–316, <https://doi.org/10.5194/gi-7-307-2018>, 2018.
707
708 Nakamura, T., Ariga, A., Ban, T., Fukuda, T., Fukuda, T., Fujioka, T., Furukawa, T.,
709 Hamada, K., Hayashi, H., Hiramatsu, S., Hoshino, K., Kawada, J., Koike, N., Komatsu,
710 M., Matsuoka, H., Miyamoto, S., Miyanishi, K., Miyanishi, M., Morishima, K., Nada,
711 H., Naganawa, N., Nakano, T., Narita, K., Natsume, M., Niwa, K., Nonaka, N., Park,
712 B. D., Sato, O., Takahashi, S., Toshito, T., Uetake, T., Nakamura, M., Kuwabara, K.,
713 Nishiyama, S., Nonoyama, Y., and Kodama, K.: The OPERA film: New nuclear
714 emulsion for large-scale, high-precision experiments, *Nucl. Instrum. Methods Phys.*
715 *Res. A*, 556, 1, 80–86, <https://doi.org/10.1016/j.nima.2005.08.109>, 2005.
716
717 Nishio, A., Morishima, K., Kuwabara, K., Yoshida, T., Funakubo, T., Kitagawa, N.,
718 Kuno, M., Manabe, Y., and Nakamura, M.: Nuclear emulsion with excellent long-term
719 stability developed for cosmic-ray imaging, *Nuclear Instruments and Methods in*
720 *Physics Research A*, 966, 163850, <https://doi.org/10.1016/j.nima.2020.163850>, 2020.
721

722 Nishiyama, R., Miyamoto, S., and Naganawa, N.: Experimental study of source of
723 background noise in muon radiography using emulsion film detectors, *Geosci. Instrum.*
724 *Methods Data Syst.*, 3, 29–39, <https://doi.org/10.5194/gi-3-29-2014>, 2014.

725

726 Nishiyama, R., Miyamoto, S., Okubo, S., Oshima, H., and Maekawa, T.: 3D density
727 modeling with gravity and muon-radiographic observations in Showa–Shinzan lava
728 dome, Usu, Japan, *Pure Appl. Geophys.*, 174, 1061–1070,
729 <https://doi.org/10.1007/s00024-016-1430-9>, 2017.

730

731 Nishiyama, R., Miyamoto, S., and Nagahara, S.: Estimation of the bulk density of the
732 Omuro scoria cone (eastern Izu, Japan) from gravity survey, *Bull. Earthq. Res. Inst.*
733 *Univ. Tokyo*, 95, 1–7, [https://repository.dl.itc.u-](https://repository.dl.itc.u-tokyo.ac.jp/record/2000093/files/IHO951401.pdf)
734 [tokyo.ac.jp/record/2000093/files/IHO951401.pdf](https://repository.dl.itc.u-tokyo.ac.jp/record/2000093/files/IHO951401.pdf), 2020.

735

736 Oláh, L., Tanaka, H. K. M., Ohminato, T., and Varga, D.: High-definition and low-noise
737 muography of the Sakurajima volcano with gaseous tracking detectors, *Sci. Rep.*, 8,
738 3207, <https://doi.org/10.1038/s41598-018-21423-9>, 2018.

739

740 Rosas-Carbajal, M., Jourde, K., Marteau, J., Deroussi, S., Komorowski, J.-C., and
741 Gibert, D.: Three-dimensional density structure of La Soufrière de Guadeloupe lava
742 dome from simultaneous muon radiographies and gravity data, *Geophys. Res. Lett.*, 44,
743 6743–6751, <https://doi.org/10.1002/2017GL074285>, 2017.

744

745 Saito, T., Takahashi, S., and Wada, H.: ^{14}C ages of Omuroyama Volcano, Izu Peninsula,

746 Bull. Volcanol. Soc. Jpn. , 48, 215–219, https://doi.org/10.18940/kazan.48.2_215, 2003.
747 (in Japanese)
748
749 Saracino, G., Amato, L., Ambrosino, F., Antonucci, G., Bonechi, L., Cimmino, L.,
750 Consiglio, L., D'Alessandro, R., De Luzio, E., Minin, G., Noli, P., Scognamiglio, L.,
751 Strolin, P., and Varriale, A.: Imaging of underground cavities with cosmic-ray muons
752 from observations at Mt. Echia (Naples), Sci. Rep., 7, 1181,
753 <https://doi.org/10.1038/s41598-017-01277-3>, 2017.
754
755 Taha, A. A., and Mohamed, A. A.: Chemical, physical and geotechnical properties
756 comparison between scoria and pumice deposits in Dhamar–Rada Volcanic Field, SW
757 Yemen, Aust. J. Basic & Appl. Sci., 7, 11, 116–124,
758 <http://www.ajbasweb.com/old/ajbas/2013/September/116-124.pdf>, 2013.
759
760 Takahashi, S., Aoki, S., Kamada, K., Mizutani, S., Nakagawa, R., Ozaki, K., and
761 Rokujo, H.: GRAINE project: The first balloon-borne, emulsion gamma-ray telescope
762 experiment, Prog. Theor. Exp. Phys., 4, <https://doi.org/10.1093/ptep/ptv046>, 2015.
763
764 Tanahashi, M., et al. (Particle Data Group), Phys. Rev. D 98, 030001,
765 <https://doi.org/10.1103/PhysRevD.98.030001>, 2018.
766
767 Tanaka, H. K. M., Nakano, T., Takahashi, S., Yoshida, J., Takeo, M., Oikawa, J.,
768 Ohminato, T., Aoki, Y., Koyama, E., Tsuji, H., and Niwa, K.: High resolution imaging
769 in the inhomogeneous crust with cosmic-ray muon radiography: The density structure

書式を変更: フォントの色 : 自動

770 below the volcanic crater floor of Mt. Asama, Japan, *Earth Planet. Sci. Lett.*, 263, 1–2,
771 104–113, <https://doi.org/10.1016/j.epsl.2007.09.001>, 2007.

772

773 Tanaka, H. K. M., Uchida, T., Tanaka, M., Shinohara, H., and Hideaki, T.: Cosmic-ray
774 muon imaging of magma in a conduit: Degassing process of Satsuma–Iwojima Volcano,
775 Japan, *Geophys. Res. Lett.*, 36, L01304, <https://doi.org/10.1029/2008GL036451>, 2009.

776

777 Tanaka, H. K. M., Taira, H., Uchida, T., Tanaka, M., Takeo, M., Ohiminato, T., and
778 Tsuji, H.: Three-dimensional computational axial tomography scan of a volcano with
779 cosmic ray muon radiography, *J. Geophys. Res. Solid Earth*, 115, B12332,
780 <https://doi.org/10.1029/2010JB007677>, 2010.

781

782 Tanaka, H. K. M., Kusagaya, T., and Shinohara, H.: Radiographic visualization of
783 magma dynamics in an erupting volcano, *Nat. Commun.*, 5, 3381,
784 <https://doi.org/10.1038/ncomms4381>, 2014.

785

786 Tioukov, V., Alexandrov, A., Bozza, C., Consiglio, L., D'Ambrosio, N., De Lellis, G., De
787 Sio, C., Giudicepietro, F., Macedonio, G., Miyamoto, S., Nishiyama, R., Orazi, M.,
788 Peluso, R., Sheshukov, A., Sirignano, C., Stellacci, S. M., Strolin, P., and Tanaka, H. K.
789 M.: First muography of Stromboli volcano, *Sci. Rep.*, 9, 6695,
790 <https://doi.org/10.1038/s41598-019-43131-8>, 2019.

791

792 Watanabe, A., Takenaka, H., Fujii, Y., and Fujiwara, H.: Seismometer azimuth
793 measurement at K-NET station (2): Oita Prefecture, *Zisin*, 53, 185–192,

794 https://doi.org/10.4294/zisin1948.53.2_185, 2000. (in Japanese)

795

796 Yamamoto, H.: The mode of lava outflow from cinder cones in the Ojika–Jima

797 monogenetic volcano group, Bull. Volcanol. Soc. Jpn., 48, 1,

798 https://doi.org/10.18940/kazan.48.1_11, 2003. (in Japanese)

799

800 Yoshimoto, M., Nakano, T., Komatani, R., and Kawahara, H.: Hyper-track selector

801 nuclear emulsion readout system aimed at scanning an area of one thousand square

802 meters, Prog. Theor. Exp. Phys., 2017, 10, <https://doi.org/10.1093/ptep/ptx131>, 2017.

803

804 **Appendix A**

805 We here consider how the position dependency of the detected tracks affects the density
806 results.

807 The fill factor of the base tracks (i.e., track detection efficiency in a film) also depends
808 on the position of the scanned film. The typical causes of the decrease of the fill factor
809 are heterogeneous thickness of the emulsion layers, some dusts or scratches on the
810 emulsion surface, and the poorly tuned parameters for the scanning.

811 Fig. 15 shows the position distribution of the fill factor of all films of an ECC. For
812 example, at upper right the films tend to have the low fill factor (e.g., a-f, h, k, l, q). This
813 part has the larger thickness of emulsion layer because the drops of glycerin solution
814 were left in the upper right corner when drying after soaking due to the structure of
815 developing racks. Fig. 15(s) and (t) have larger area of low fill factor in the right and left.
816 The reason might be the poorly tuned parameters for the scanning.

817 Compared to the size of the scoria cone, the ECC is a very small “element”, thus the
818 local position dependence of the fill factor can be approximately treated as an average
819 fill factor $\varepsilon_j(\theta_x, \theta_y)$. The decrease of the fill factor is reflected in the $\varepsilon_j(\theta_x, \theta_y)$ in Eq. (4).
820 Finally, $\varepsilon_j(\theta_x, \theta_y)$, which encompasses the effects of the local decrease of the fill factor, is
821 effectively used to derive the angle-dependent muon detection efficiency.

822 We should also consider the position dependency of noise. Local high density of random
823 silver grains caused by any chemical conditions, or fake images produced by scratches
824 on the films tend to create a group of fake tracks concentrated in one place. In addition,
825 such fake tracks tend to have small slopes by scanning with automated emulsion readout
826 system. If such noise is continuous at the same location on the film, they might make
827 many parallel tracks at a certain slope and give a systematic error in the result. However,
828 such possibility has been eliminated by the track selection algorithm described in the
829 section 4.2. Because such concentrated tracks in position and angular space make
830 numerous branches in track connection (see Fig. 6) and tracks with such branches were
831 removed in the selection procedure. Fig. 16 shows the number of selected tracks with
832 small slope per mm^2 in each observation site. The histogram roughly fits the Poisson
833 distribution and there is no remarkable excess. The difference of the peak in the
834 histograms depends on the difference of exposure time (SE, W, NNE), existence of
835 topography in the backward direction (NE), pitch angle of the detector attitude (e.g., SW
836 has larger pitch angle, thus less tracks of the small slopes from the backward direction),
837 and the difference of muon detection efficiency.

コメントの追加 [宮本 成悟13]: I've added the appendix for RC2

書式を変更: フォントの色 : 自動

書式を変更: フォントの色 : 自動

書式を変更: フォントの色 : 自動

書式を変更: フォントの色 : 自動

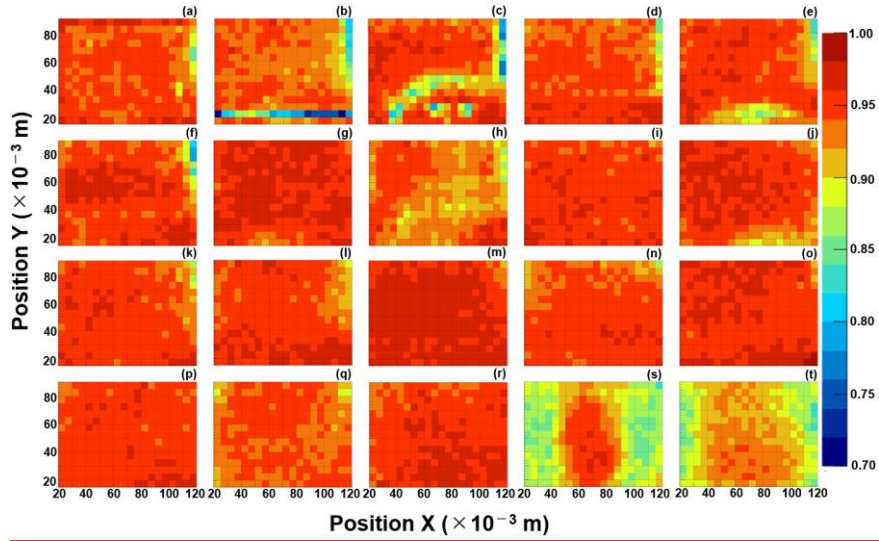
書式を変更: フォントの色 : 自動

書式を変更: フォントの色 : 自動

書式を変更: フォントの色 : 自動, 上付き

書式を変更: フォントの色 : 自動

838



839

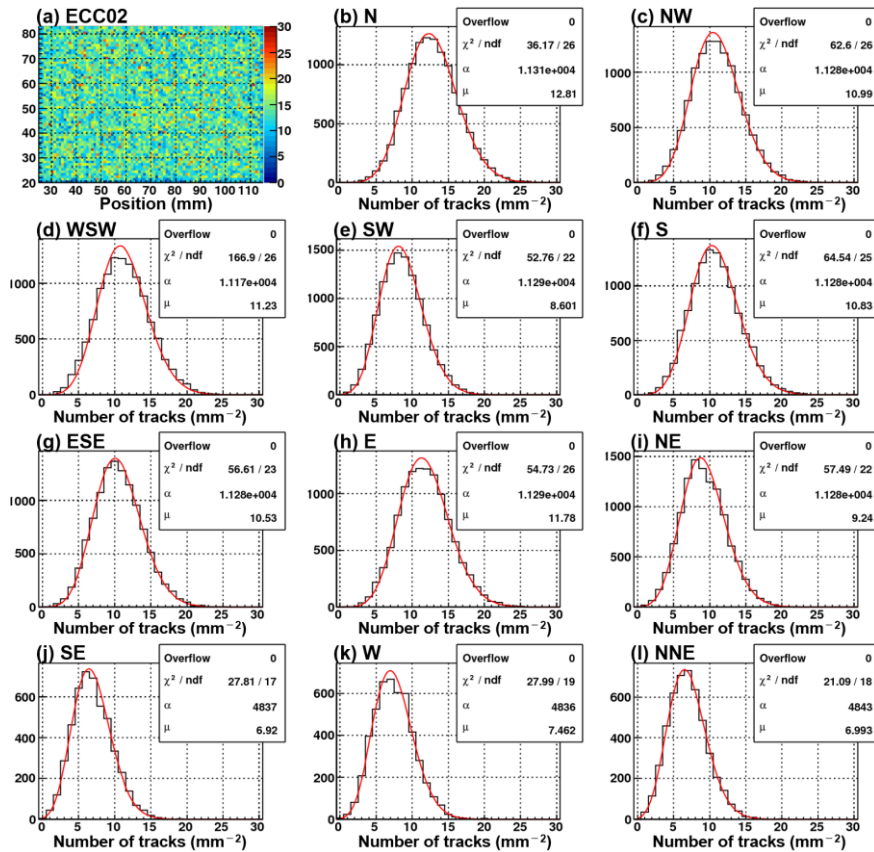
840

841 Figure 15. The position distribution of the fill factor in each film of ECC02. (a)–(t)

842 represent PL01–PL20, respectively.

843

書式を変更: フォントの色 : 自動



- 書式を変更: フォントの色 : 自動
- 書式を変更: フォントの色 : 自動
- 書式を変更: 上付き
- 書式を変更: フォントの色 : 自動
- 書式を変更: フォントの色 : 自動, 上付き/下付き (なし)
- 書式を変更: フォントの色 : 自動
- 書式を変更: フォントの色 : 自動, 上付き/下付き (なし)
- 書式を変更: フォントの色 : 自動
- 書式を変更: フォント : +本文のフォント (Century), フォントの色 : 自動
- 書式を変更: フォントの色 : 自動
- 書式を変更: フォント : +本文のフォント (Century), フォントの色 : 自動
- 書式を変更: フォントの色 : 自動
- 書式を変更: フォントの色 : 自動
- 書式を変更: フォントの色 : 自動
- 書式を変更: フォント : +本文のフォント (Century), フォントの色 : 自動
- 書式を変更: フォントの色 : 自動
- 書式を変更: フォントの色 : 自動
- 書式を変更: フォントの色 : 自動
- 書式を変更: フォントの色 : 自動
- 書式を変更: フォントの色 : 自動

845

846

847 Figure 16. (a) The position distribution of the number of the selected tracks per mm² in
 848 the ECC02. (b)–(l) The number of the selected tracks per mm² (the black line) with the
 849 fitting result of Poisson distribution ($= \alpha \mu^x e^{-\mu} / x!$, the red line) in each observation
 850 site, respectively. The tracks selected for this figure came from in the backward
 851 direction and have small slopes ($|\tan \theta_x| < 0.5$ and $|\tan \theta_y| < 0.5$).

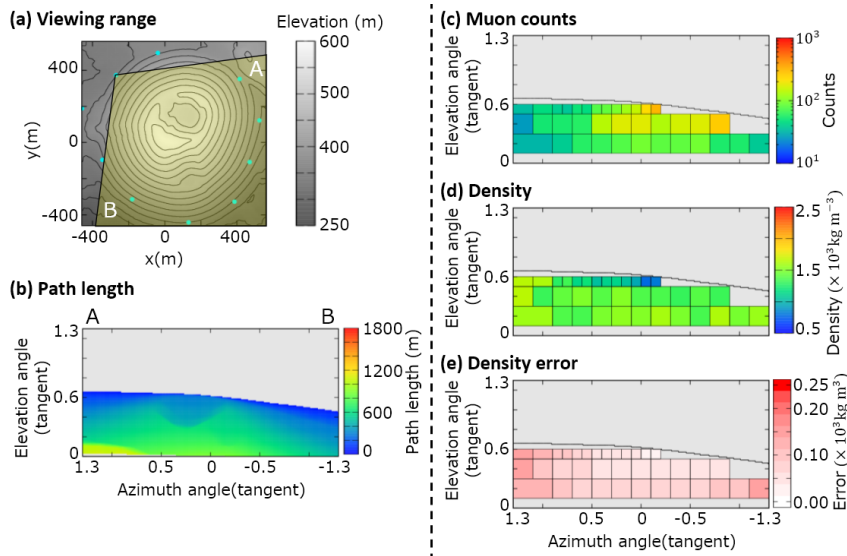
852

853

854 **Appendix B**

855 The density results for each observation site are shown in Figs 17–26.

856



857

858

859 Figure 17. Observation site NW. (a) Map, topography, and viewing range; (b) path

860 length of the volcanic cone; (c) muon counts N_i^{obs} ; (d) density ρ_i . The maximum value of

861 the color bar indicates a density of $>2.5 \times 10^3 \text{ kg m}^{-3}$ and the minimum value is <0.5

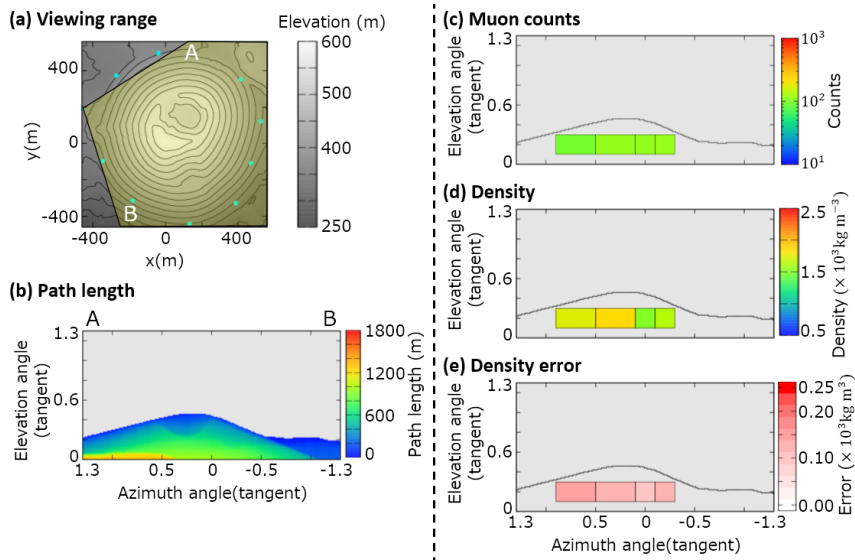
862 $\times 10^3 \text{ kg m}^{-3}$. (e) Density error $\Delta\rho = (\rho_i^{up} - \rho_i^{low})/2$. The maximum value of the color

863 bar indicates a density error of $>0.25 \times 10^3 \text{ kg m}^{-3}$.

864

書式を変更: フォントの色 : 自動

865



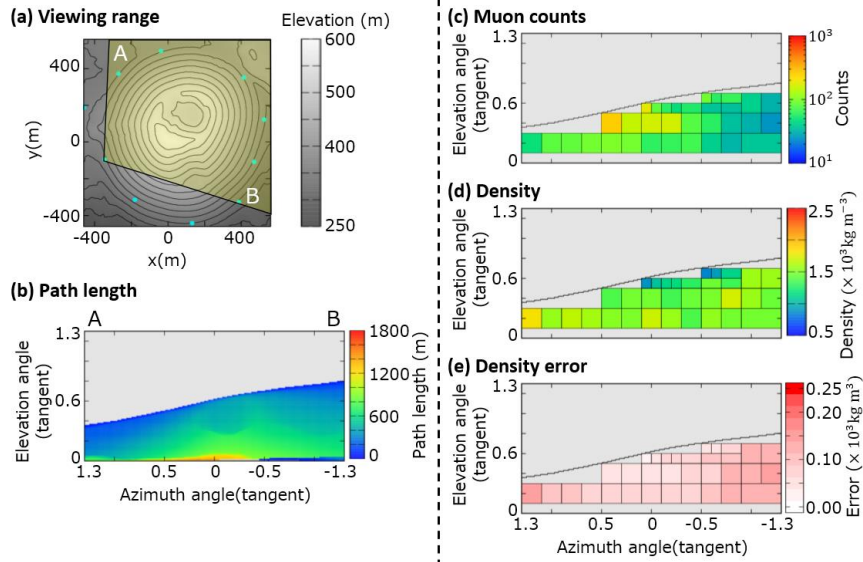
866

867

868 Figure 18. Observation site W. (a) Map, topography, and viewing range; (b) path
 869 length of the volcanic cone; (c) muon counts N_i^{obs} ; (d) density ρ_i . The maximum value of
 870 the color bar indicates a density of $>2.5 \times 10^3 \text{ kg m}^{-3}$ and the minimum value is <0.5
 871 $\times 10^3 \text{ kg m}^{-3}$. (e) Density error $\Delta\rho = (\rho_i^{up} - \rho_i^{low})/2$. The maximum value of the color
 872 bar indicates a density error of $>0.25 \times 10^3 \text{ kg m}^{-3}$.

873

874



875

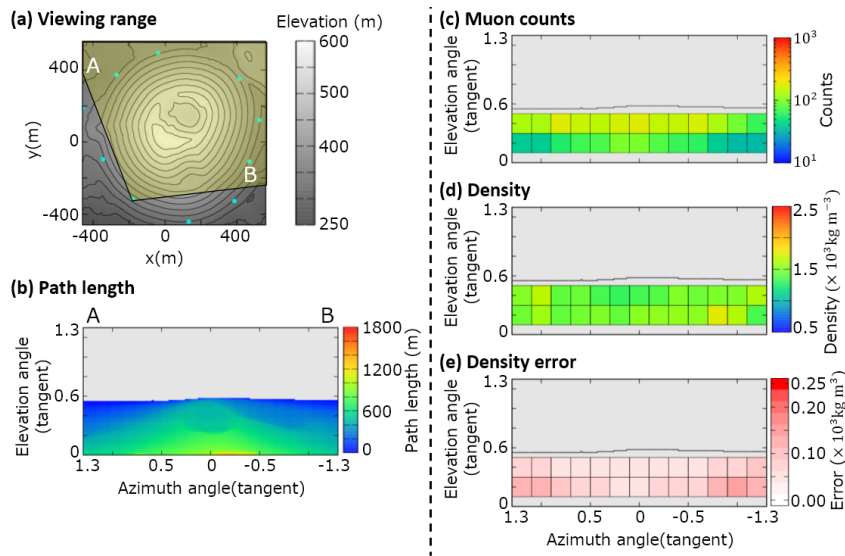
876

877 Figure 19. Observation site WSW. (a) Map, topography, and viewing range; (b) path
 878 length of the volcanic cone; (c) muon counts N_i^{obs} ; (d) density ρ_i . The maximum value of
 879 the color bar indicates a density of $>2.5 \times 10^3 \text{ kg m}^{-3}$ and the minimum value is <0.5
 880 $\times 10^3 \text{ kg m}^{-3}$. (e) Density error $\Delta\rho = (\rho_i^{up} - \rho_i^{low})/2$. The maximum value of the color
 881 bar indicates a density error of $>0.25 \times 10^3 \text{ kg m}^{-3}$.

882

883

884



885

886

887 Figure 20. Observation site SW. (a) Map, topography, and viewing range; (b) path
 888 length of the volcanic cone; (c) muon counts N_i^{obs} ; (d) density ρ_i . The maximum value of
 889 the color bar indicates a density of $>2.5 \times 10^3 \text{ kg m}^{-3}$ and the minimum value is <0.5
 890 $\times 10^3 \text{ kg m}^{-3}$. (e) Density error $\Delta\rho = (\rho_i^{up} - \rho_i^{low})/2$. The maximum value of the color
 891 bar indicates a density error of $>0.25 \times 10^3 \text{ kg m}^{-3}$.

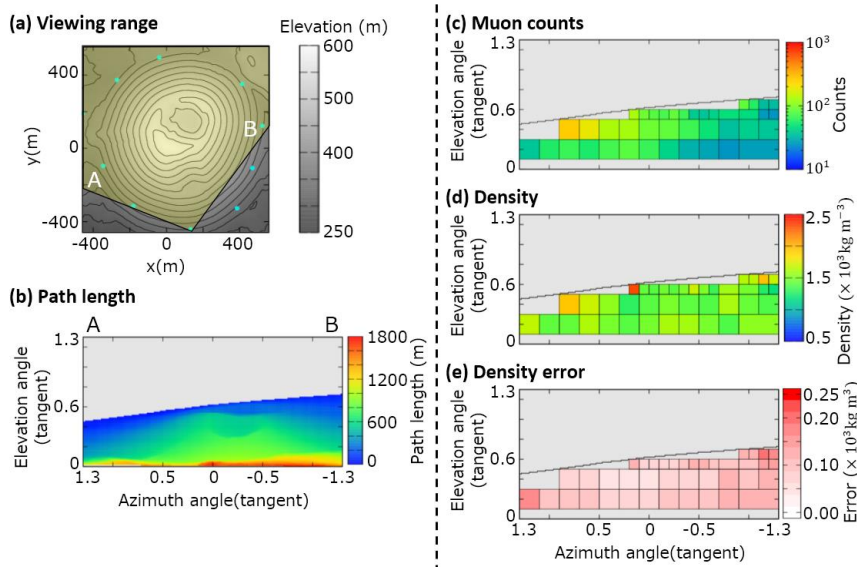
892

893

894

895

896



897

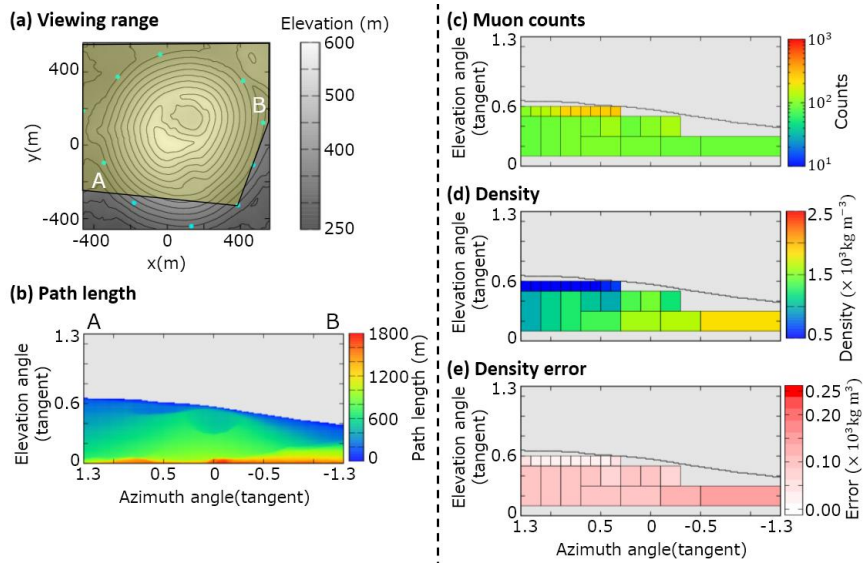
898

899 Figure 21. Observation site S. (a) Map, topography, and viewing range; (b) path
 900 length of the volcanic cone; (c) muon counts N_i^{obs} ; (d) density ρ_i . The maximum value of
 901 the color bar indicates a density of $>2.5 \times 10^3 \text{ kg m}^{-3}$ and the minimum value is <0.5
 902 $\times 10^3 \text{ kg m}^{-3}$. (e) Density error $\Delta\rho = (\rho_i^{up} - \rho_i^{low})/2$. The maximum value of the color
 903 bar indicates a density error of $>0.25 \times 10^3 \text{ kg m}^{-3}$.

904

905

906



907

908

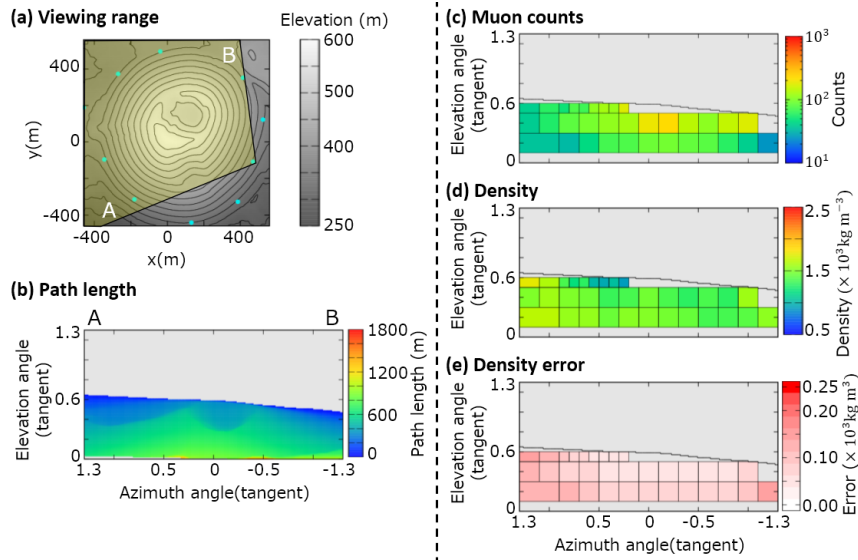
909 Figure 22. Observation site SE. (a) Map, topography, and viewing range; (b) path
 910 length of the volcanic cone; (c) muon counts N_i^{obs} ; (d) density ρ_i . The maximum value of
 911 the color bar indicates a density of $>2.5 \times 10^3 \text{ kg m}^{-3}$ and the minimum value is <0.5
 912 $\times 10^3 \text{ kg m}^{-3}$. (e) Density error $\Delta\rho = (\rho_i^{up} - \rho_i^{low})/2$. The maximum value of the color
 913 bar indicates a density error of $>0.25 \times 10^3 \text{ kg m}^{-3}$.

914

915

916

917



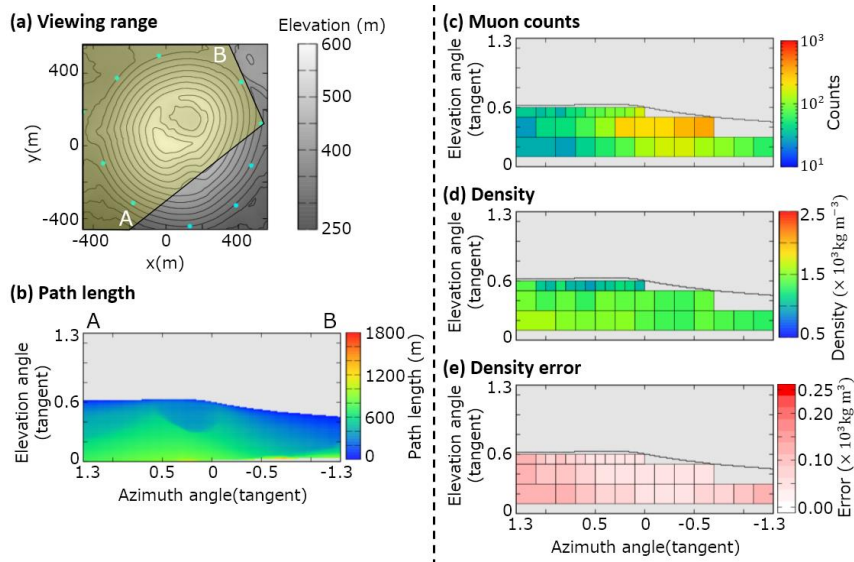
918

919

920 Figure 23. Observation site ESE. (a) Map, topography, and viewing range; (b) path
921 length of the volcanic cone; (c) muon counts N_i^{obs} ; (d) density ρ_i . The maximum value of
922 the color bar indicates a density of $>2.5 \times 10^3 \text{ kg m}^{-3}$ and the minimum value is <0.5
923 $\times 10^3 \text{ kg m}^{-3}$. (e) Density error $\Delta\rho = (\rho_i^{up} - \rho_i^{low})/2$. The maximum value of the color
924 bar indicates a density error of $>0.25 \times 10^3 \text{ kg m}^{-3}$.

925

926



927

928

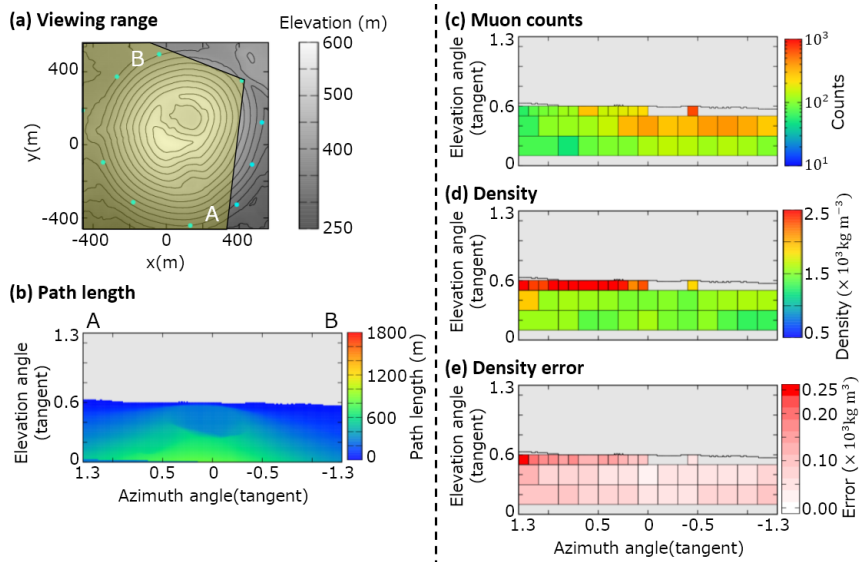
929 Figure 24. Observation site E. (a) Map, topography, and viewing range; (b) path
930 length of the volcanic cone; (c) muon counts N_i^{obs} ; (d) density ρ_i . The maximum value of
931 the color bar indicates a density of $>2.5 \times 10^3 \text{ kg m}^{-3}$ and the minimum value is <0.5
932 $\times 10^3 \text{ kg m}^{-3}$. (e) Density error $\Delta\rho = (\rho_i^{up} - \rho_i^{low})/2$. The maximum value of the color
933 bar indicates a density error of $>0.25 \times 10^3 \text{ kg m}^{-3}$.

934

935

936

937



938

939

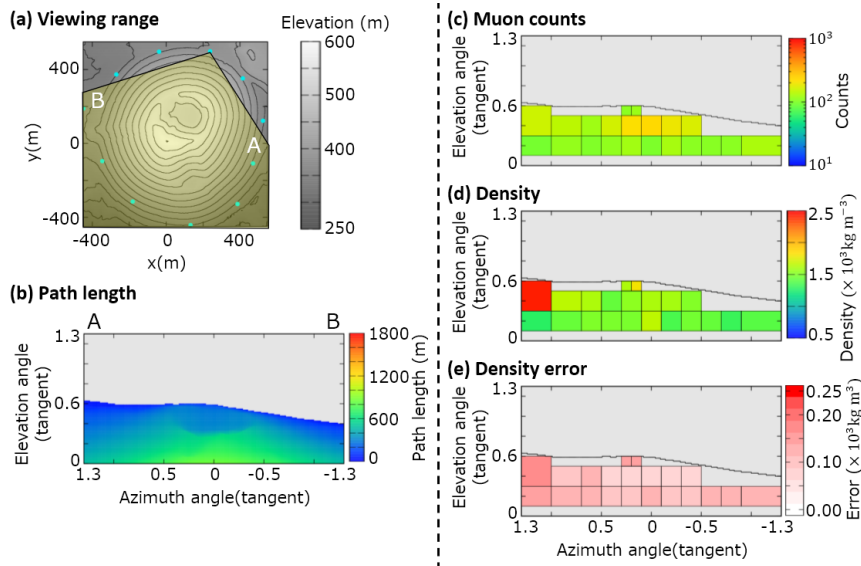
940 Figure 25. Observation site NE. (a) Map, topography, and viewing range; (b) path
 941 length of the volcanic cone; (c) muon counts N_i^{obs} ; (d) density ρ_i . The maximum value of
 942 the color bar indicates a density of $>2.5 \times 10^3 \text{ kg m}^{-3}$ and the minimum value is <0.5
 943 $\times 10^3 \text{ kg m}^{-3}$. (e) Density error $\Delta\rho = (\rho_i^{up} - \rho_i^{low})/2$. The maximum value of the color
 944 bar indicates a density error of $>0.25 \times 10^3 \text{ kg m}^{-3}$.

945

946

947

948



949

950

951 Figure 26. Observation site NNE. (a) Map, topography, and viewing range; (b) path
 952 length of the volcanic cone; (c) muon counts N_i^{obs} ; (d) density ρ_i . The maximum value of
 953 the color bar indicates a density of $>2.5 \times 10^3 \text{ kg m}^{-3}$ and the minimum value is <0.5
 954 $\times 10^3 \text{ kg m}^{-3}$. (e) Density error $\Delta\rho = (\rho_i^{up} - \rho_i^{low})/2$. The maximum value of the color
 955 bar indicates a density error of $>0.25 \times 10^3 \text{ kg m}^{-3}$.

956

957